FACULTY OF HEALTH SCIENCES
UNIVERSITY OF COPENHAGEN

Rigshospitalet

Estimation of right ventricular ejection fraction using first-pass FDG-PET imaging

Andreas Ettrup Clemmensen

Master of Science in Engineering
Copenhagen, June 2012
IMM-MSc-2012-47

DTU Informatics
Department of Informatics and Mathematical Modelling

University of Copenhagen
Cluster for Molecular Imaging
Faculty of Health and Medical Sciences
Building 12.3, Blegdamsvej 3b
DK-2200 Copenhagen, Denmark
bmi.ku.dk/english/

Technical University of Denmark
Informatics and Mathematical Modelling
Building 321, DK-2800 Kongens Lyngby, Denmark
Phone +45 45253351, Fax +45 45882673
www.imm.dtu.dk

Department of Clinical Physiology, Nuclear Medicine and PET
Rigshospitalet, KF-3982
Blegdamsvej 9, DK-2100 Copenhagen, Denmark
Phone +45 35453919, Fax +45 35453898
http://www.rigshospitalet.dk/

IMM-MSc-2012-47

SUBMITTED IN PARTIAL FULFILLMENT OF THE
REQUIREMENTS FOR THE DEGREE OF

MASTER OF SCIENCE
IN
BIOMEDICAL ENGINEERING

AT
THE UNIVERSITY OF COPENHAGEN
AND
THE TECHNICAL UNIVERSITY OF DENMARK

Supervised by

Professor, MD, PhD, DMSc Andreas Kjær
University of Copenhagen, Rigshospitalet

Professor, PhD Rasmus Larsen
Technical University of Denmark

Professor, PhD Knut Conradsen
Technical University of Denmark

Copenhagen, 1 June 2012

Andreas Ettrup Clemmensen

Summary

The right ventricular ejection fraction (RVEF) is an important diagnostic marker, but its complex shape, placement and contraction pattern makes estimations of its viability challenging. Different modalities is used for estimating RVEF, with first-pass radionuclide ventriculography (RNV) as one of the most precise and reliable modalities. Using a gamma camera, the tracer bolus is imaged during the initial passage where it is confined to the right side of the heart.

This project investigates the possibility of transferring this first-pass concept to positron emission tomography (PET), which has superior sensitivity and the potential of sparing patient for an extra examination. 13 patients referred to a FDG-PET scan at Rigshospitalet were scanned in list-mode during the infusion of FDG. After initial estimations of arrival and transit time of the first-pass bolus in the heart, ECG-gated reconstructions of 4-6 second were made. An ROI covering the right ventricle was drawn, and from time-activity curves, the RVEF was estimated.

The developed method significantly underestimates RVEF, which is most likely due to imprecise ROI drawing. Indications of a correlation between the RVEF values by PET and cMRI is found, but further improvements of the estimation by PET are required before any conclusions can be drawn.

Resumé

Højre ventrikels funktion er en vigtig diagnostisk markør i flere sammenhænge, men struktur og sammentrækningsmønster gør det vanskeligt at bestemme uddrivelsesfraktionen. Idag benyttes flere forskellige metoder, såsom ultralyd og første passage isotopventrikulografi. Sidstnævnte udnytter at sporstoffet kun befinder sig i højre side af hjertet under første gennemløb, og dermed undgår man signal fra venstre side.

Det nærværende projekt undersøger mulighederne for at overføre første passage konceptet til PET, som bruges i en lang række rutinemæssige undersøgelser. Dermed kan yderligere skanninger forhåbentlig overflødiggøres. 13 patienter henvist til FDG-PET skanning på Rigshospitalet blev skannet under injektion af bolus, og fik ydermere foretaget cMRI skanning til brug som reference.

Den udviklede metode undervurderer uddrivelsesfraktionen betydeligt, hvilket formentlig kan henføres til at højre ventrikel ikke er afgrænset korrekt i forhold til atriet. Der ses en indikation af korrelation mellem værdierne fundet med FDG-PET og dem målt med cMRI, dog skal metoden forberedes før endelige konklusioner kan drages.

Preface

The present thesis represents the mandatory master project under the Master of Science in Engineering education Medicine & Technology offered jointly by the Technical University of Denmark (DTU) and University of Copenhagen (KU).

The project was carried out at Cluster for Molecular Imaging (CMI) at Faculty of Health and Medical Sciences at University of Copenhagen and Rigshospitalet, as well at the Department of Informatics and Mathematical Modelling (IMM) at the Technical University of Denmark. The work began in January 2012, and ended in June within the same year with an assigned workload of 30 ECTS points.

Acknowledgements

I owe my absolute gratitude to my supervisors, professor, MD, PhD, DMSc Andreas Kjær, professor, PhD Rasmus Larsen and professor, PhD Knut Conradsen for this opportunity, their calm guidance and always seeing the big picture. It has been a privilege working with you, one I hope to continue.

The warmest thanks go to PhD student, MSc Carsten Haagen Nielsen for continuous inspiration and discussions on both the project and life in general. For creating a youthful atmosphere and creative environment at the office, Karina, Kamilla and Sofie have been second to none, and I continue to be amazed by the energy and joy of the people at CMI. A weekly highlight, both academic and socially, has been the Friday meetings at DTU. I shall miss those.

Several people have aided and guided me during the course of this project. Merence Sibomana and PhD Flemming Littrup Andersen shared some of their great technical knowledge. MSc Anders Nymark Christensen and MSc Martin Lyngby Lassen have kindly assisted me with hands-on experience on equipment and numerous good advice. Great appreciation go to professor, head of department, MD, DMSc Liselotte Højgaard for her enduring work of providing state-of-the-art facilities.

There are no words that can describe my appreciation of my elite study group, Charlotte, Martin and Michael, who have put up with me for almost six years and, if any, made me reach this far. Finally, I am forever indebted to my loving parents and siblings, who have always supported and encouraged me in every step. Thank you.

> *quasi nanos, gigantium humeris insidentes, ut possimus plura eis et remotiora videre* - Bernard of Chartres

Contents

Nomenclatures

Abbreviations

ANOVA	Analysis of variance
b-TFE	balanced Turbo Field Echo
bpm	beats per minute
cCT	cardiac Computed Tomography
cMRI	cardiac Magnetic Resonance Imaging
CO	Cardiac Output
CT	Computed Tomography
DICOM	Digital Imaging and Communications in Medicine
ECG	Electrocardiogram
EDV	End-diastolic volume
ESV	End-systolic volume
FBP	Filtered Back Projection
FOV	Field Of View
GLUT	Glucose transport protein
LOR	Line of Response
LSO	Lutetium Oxyorthosilicate
OSEM	Ordered-Subset Expectation Maximization
PE	Pulmonary Embolism
PET	Positron Emission Tomography
PMT	Photo Multiplier Tube
PTT	Pulmonary Transit Time
RNV	Radionuclide ventriculography
ROI	Region of Interest

RVEF	Right Ventricular Ejection Fraction
RVV	Right Ventricular Viability
SV	Stroke Volume
TAC	Time-Activity Curve
TR	Echo time
TR	Repetition time

Symbols

β^+	Positron
γ	Photon
$\Gamma(\alpha)$	Gamma function
λ	Poisson intensity parameter
μ	Linear Attenuation Coefficient
τ	Coincidence window
c	Speed of light
E	Energy
f	Image
I	Photon flux
M	Cost matrix
m	Mass
R	Euler rotation matrix
s	Projection data
v	Neutrino

1

Introduction

During his work at the University of Copenhagen in the early 1920s, Hevesy [26] conceived *the tracer principle*, a concept he later received the Nobel Prize for. Since then, the field of medical diagnostics has increasingly embraced this paradigm, and combined with the modern aspects of technology, it continues to provide physicians with more accurate and detailed information about pathologies.

Being one of the fastest developing modalities since Röntgens X-rays, the functional information obtained by *Positron Emission Tomography* (PET) have, combined with the anatomical precision of *Computed Tomography* (CT) [3], become essential aspects of modern medicine, ranging from oncology over neurology to cardiology. In only a decade, PET examinations has gone from being an experimental research tool to standard equipment at all modern hospitals.

While PET has been the dominant modality in neurology and oncology, cardiology has, except from a few applications, been reluctant to adopt the technique. Traditionally, the gamma camera is used for cardiac imaging in nuclear medicine. Meanwhile, competing modalities have emerged in the field of cardiac diagnostics, and the obvious question presents itself: Has the possibilities in PET for cardiology been exhaustingly pursued?

1.1 Clinical motivation

The majority of cardiac examinations seek to evaluate either perfusion of the myocardium or the functional state of the heart, known as viability. *Right ventricular viability* (RVV) covers the contractile ability of the right ventricle, and is often quantified by the *right ventricular ejection fraction* (RVEF). This quantitative measure,defined in equation 1.1, is relevant in several pathological states and has been shown to have significant prognostic value [4, 16, 18].

$$RVEF = \frac{SV}{EDV} = \frac{EDV - ESV}{EDV} \tag{1.1}$$

where SV designates stroke volume, EDV and ESV is end-diastolic and end-systolic volumes, respectively.

Several pulmonary diseases, such as pulmonary embolism, can affect the function of the right ventricle, but chemotherapy given as part of cancer treatment can also be highly cardiotoxic. In the latter case, the degree of cardiac impairment is important to evaluate in order to maximize the chemo effects. However, the complex morphology of the right ventricle and dominant behaviour by big-brother left ventricle makes assessment of RVV difficult [27, 4]. The most widely used current modalities are described and discussed below:

Echocardiography Cardiac ultrasound examinations are performed routinely on almost every hospital at a daily basis, and provides an inexpensive and quick cardiac viability estimate with no patient risk. For these reasons, this modality is often the first choice for general examinations of RVV. Unfortunately, the result is semi-quantitative and highly operator-specific, and hence has poor reproducibility and certainty. Furthermore, not all patients can be adequately examined due to anatomical variation. [22, 4]

Radionuclide ventriculography (RNV) is the current clinical choice for estimating RVV using nuclear medicine, with either an equilibrium or, preferably, a first-pass approach. Technetium-99^m labelled erythrocytes are infused, and the distribution is imaged using a traditional gamma camera. The technique is hampered by relatively poor spatial resolution and signal-to-noise ratio, and can not easily be combined with other examinations. [25, 20, 11]

Cardiac computed tomography (cCT) Recent development in x-ray hardware has made CT scanners fast enough to capture cardiac motion, and hence estimate RVV on anatomical basis. This is only possible on newest generations of scanners however, and exposes the patient to ionizing radiation. Furthermore, this modality requires cardiac gating, and occasionally, contrast agents. [1]

Cardiac magnetic resonance imaging (cMRI) is currently considered the gold standard for RVEF estimation, cMRI yields high accuracy and reproducibility. It poses no ionizing radiation on the patient, but can not be used on special patient groups, such as pacemaker patients, due to the strong magnetic field. MRI is an expensive modality, time-consuming, requires highly trained technicians and the availability is limited. [2, 4]

1.2 Present project

From the previous section, it should be clear that despite clinical motivation, no perfect modality for estimating RVV yet exists [38]. This project aims to investigate the possibility of exploiting a normal FDG-PET scan conducted for other purposes as a way to obtain information about cardiac viability, specifically RVEF. Typically, the patient is injected with the FDG tracer and then waits for about an hour for it to be distributed in the body before the scan is initiated. The key idea in this project is to do a dynamic, list-mode scan during infusion of the tracer, and from that estimate the RVEF. Utilizing the first-pass idea from RNV, the tracer distribution is sampled temporally fast through the heart passage, where it is confined to the right side, avoiding spill-over effects from the left side. The superior spatial resolution of PET seems promising in this matter.

As will be elaborated in section 4.4, this approach has, to the best of knowledge, only been attempted in animals, using research dedicated MicroPET scanners. Although some success has been reported, the approach faces several challenges; the *pulmonary transit time* (PTT) is in the order of some seconds, limiting the evaluation time to this period. Furthermore, to evaluate the cardiac contraction, high temporal sampling must be applied, which is not possible on the clinical system offhand. These problems are somewhat eased by the first-pass approach, and will be addressed in this thesis.

To summarise, the goals of the project are

- **to establish a simple, robust routine for evaluating RVEF using dynamic list-mode FDG-PET scanning and correlate the estimates with those found by cardiac MRI,**
- **and to investigate the effect of different parameters for this routine, such as reconstruction algorithm.**

2

The human heart

This section presents a brief introduction to the anatomy and physiology of the human heart.

2.1 Anatomy

The heart is a slightly pointy, oblong organ of specialised fibromuscular tissue enclosed in a fibrous sack, located in the middle mediastinum, with about two-thirds of the mass to the left of the sagittal plane. It is surrounded bilaterally by the lungs, anteriorly by the sternum and posterior by the spline. The heart has an average size of about 12 x 8 x 6 cm and it weighs about 250 to 300 grams in females and males, respectively. [49]

The heart is divided into physiologically separate halves, the right and left side, and each side is subdivided into two chambers, the atrium and ventricle. This is illustrated in figure 2.1. The two sides are separated by a muscular wall called the *interventricular septum*, and the chambers are completely separated by connective tissue called the *atrioventricular septum*, except by at one point on each side; an orifice hosting the tricuspide and mitral valve on right and left side, respectively.

The *superior and inferior vena cava* returns the de-oxygenated blood from the body, and empty into the right atrium. From the right ventricle departs the *pulmonary trunk*, which quickly divides into the left and right *pulmonary ateries*, supplying the lungs with blood. The oxygenated blood is then returned to the left atrium by the pulmonary veins, and leaves the left ventricle through the *aorta*.

The atrioventricular septums are, for practical uses, in line across the heart, but inclined forward and to the left to the sagittal plane at about 45°. Hence, the logical planes of the heart are different from the traditional orientation of the body, giving rise to some confusion. To encounter this, the American Heart Association has established a convention

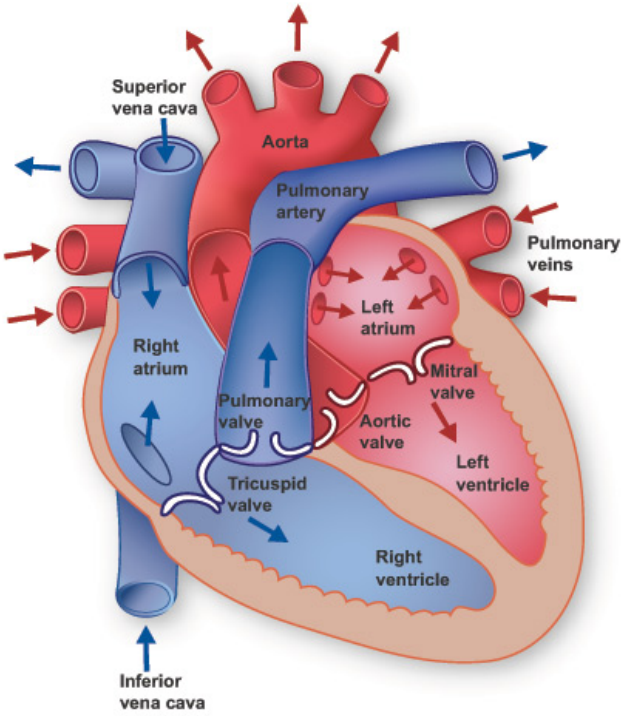

Figure 2.1 – Overview of the chambers in the human heart, shown in anterior aspect. Right side of the heart is blue, illustrating de-oxygenated blood returning from the systemic circuit and pumped to the lungs. The left side is red, indicating blood full of oxygen coming from the lungs and pumped out in the body. Arrows indicate the direction of the primary blood flow. From [51]

for reorienting medical images of the heart, as described in figure 2.2 [9]. The *long-axis* of the heart is defined as the line along the left ventricle, passing through the apex and the center of the mitral valve. Hence, the obtained images are transformed as described in section 4.2, so that the long axis of the body is rotated into the cardiac long axis.

2.2 Physiology

The right side distributes de-oxygenated blood returning from the systemic circulation into the pulmonary circuit, and the left side pumps oxygenated blood out through the systemic circuit. As the peripheral resistance is much higher in the systemic arteries, the left ventricle delivers a pressure of more than 5 times that of the right ventricle, which

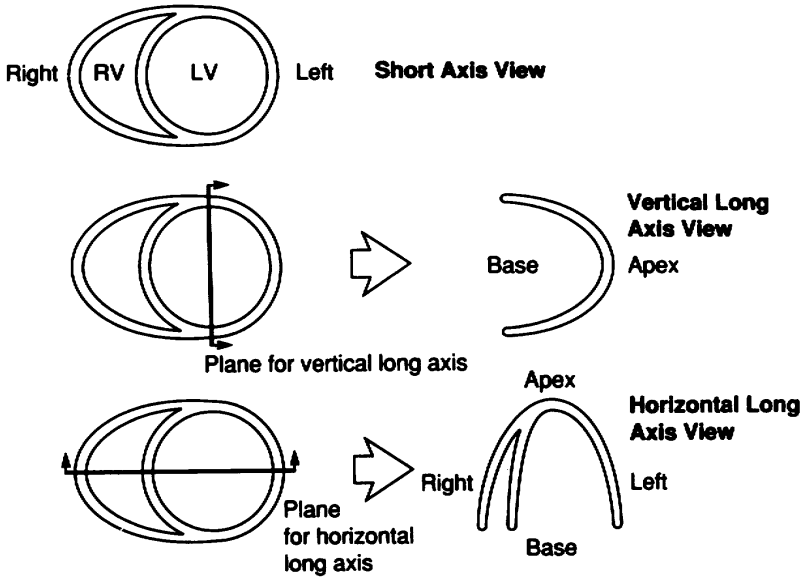

Figure 2.2 – Illustration of the convention for viewing images of the heart in medical imaging. The images are re-oriented along the long-axis of the left ventricle, with the short-axis view perpendicular to this axis used in cardiac imaging. From [9].

makes the myocardium about three times as thick, as shown in figure 2.3 [49].

The cardiac cycle is periodic, and each period is subdivided into two phases; the *systole* where the ventricles contract and blood is ejected, and the *diastole* where the heart is relaxed and being filled. The cardiac cycle and the two phases are illustrated in figure 2.4 along with the electrical signals recorded from muscular activity, known as the *electrocardiogram* (ECG).

The systole onset comes from the electrical signal of the *atrioventricular* (AV) node, which causes depolarisation of the myocardium through the bundle of Hiss along the intraventricular septum. This depolarisation is clearly visible on the ECG as the QRS complex, with the R peak having the highest amplitude. The initial part of the systole is isovolumetric, thereby increasing pressure, followed by blood ejaculation. As the contraction completes, the fraction of the EDV ejected is the ejection fraction, defined by equation 1.1. The ventricular volume during the cardiac cycle is illustrated in figure 2.5.

The heart is a highly balanced pumping mechanism, and to a large extent self-regulating. Sophisticated nervous and endocrine systems affects both the heart rate and ventricular contractility, enabling the *cardiac output* (CO) to be increased as much as five-fold compared to resting levels. Another equally important system for controlling the balance of

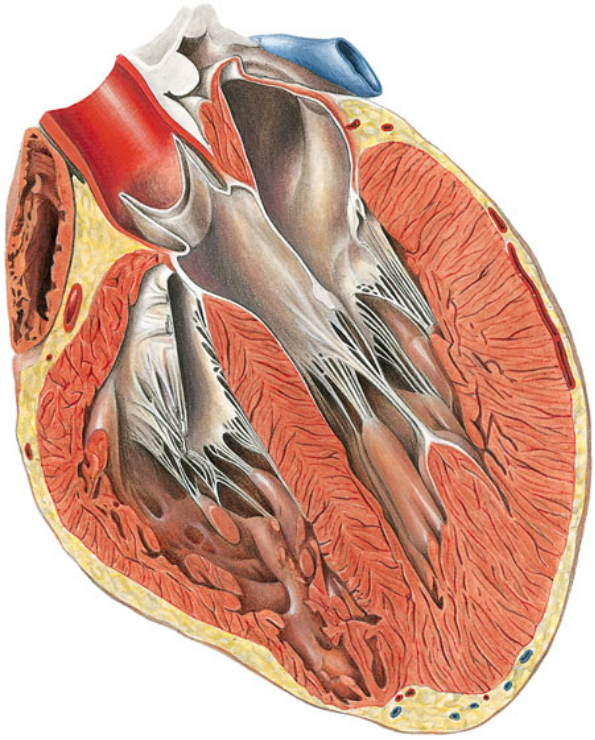

(a) Anterior aspect.

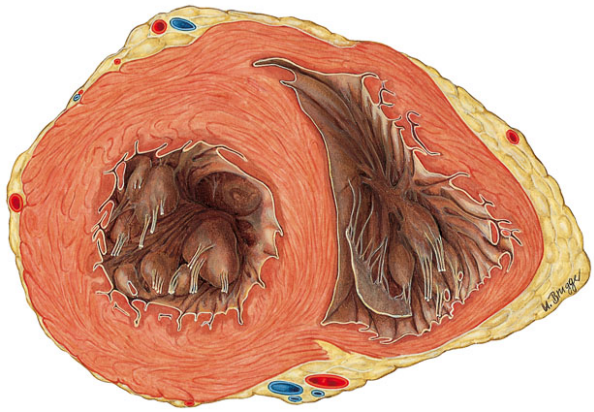

(b) Short-axis view.

Figure 2.3 – Cross sections of the right and left ventricle, showing the dominant role of the left ventricle. From [48].

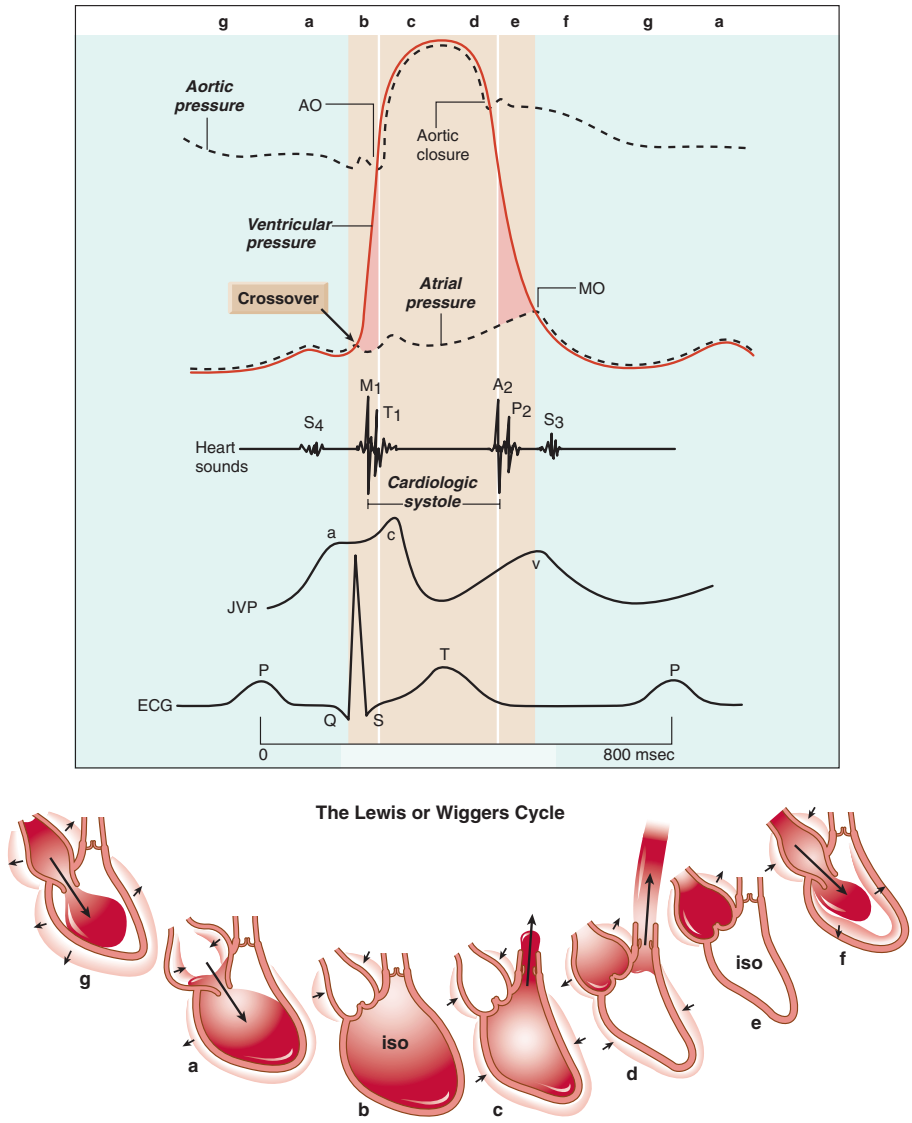

Figure 2.4 – Illustration of the cardiac contraction cycle in a so-called *Wiggers diagram*. The focus is on the left ventricle, but the mechanical processes are similar in the right side, exept for a lower absolute pressure. **a)** Arterial contraction, **b)** Iso-volumetric ventricular contraction, **c)** Ventricular contraction, **d)** Ventricular relaxation and expansion, **e)** Iso-volumetric ventricular relaxation, **f)** Early, rapid ventricular filling, **g)** Slow ventricular filling, *diastasis*. From [6].

the heart, is known as the *Frank-Starling mechanism*. In short, this states that increased ventricular filling, known as *preload*, results in more forceful contraction of the heart, hence increased SV. To some extent, this keeps the heart balanced: if one side for some reason ejects less or more blood, the Frank-Starling mechanism corrects for it, as the venous return will change accordingly. Conversely, an increased arterial pressure, in this context *afterload*, will work against blood ejection. [53]

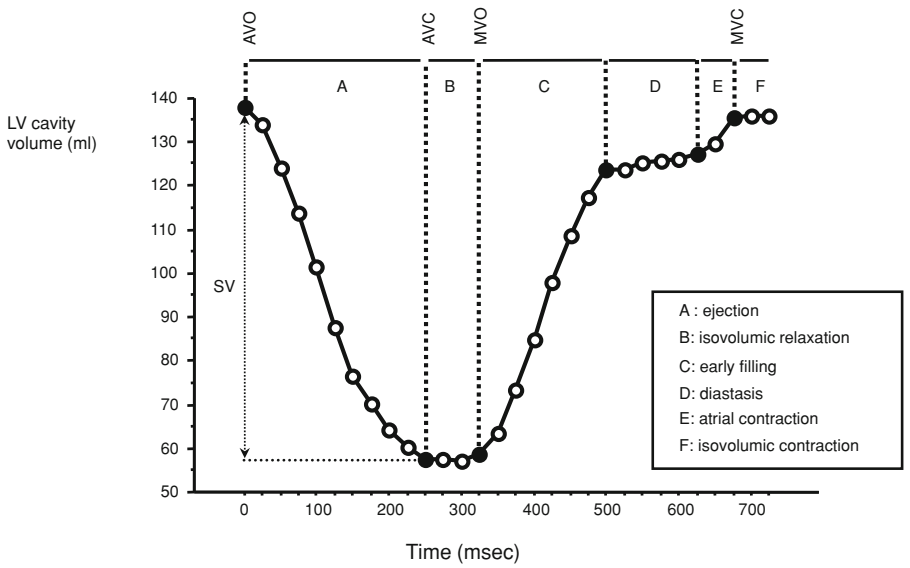

Figure 2.5 – Volume of the left ventricle during the cardiac cycle. Obtained using MRI from a young, healthy aldult female. From [5].

Several pathological states influence the cardiovascular system, with myocardial infarction and congestive heart failure being the primary causes of death in the western world. The most widespread cardiovascular pathologies initially affect the left side of the heart, but one of the more common and serious diseases to indirectly affect the right side is *pulmonary embolism* (PE). Calcifications in systemic veins can dislodge and cause occlusion in the narrow pulmonary arterioles, which, depending on the degree of blocking, can cause increased right ventricular afterload or acute circulatory failure. RVEF has been shown to be one of the best markers to predict survival and overall outcome of these diseases [18, 16, 4].

3

Positron Emission Tomography

This section describes the fundamental principles of *Positron Emission Tomography* (PET). The modality was proposed by Phelps et al. [41], but it was not until the combination with a CT scanner it reached the popularity it receives today [31]. Although there are several technical differences, PET inherited much of the early technology from the CT scanner.

3.1 Nuclear emission

PET imaging begins with the nuclear decay in the tracer molecule, where certain radionuclide with a low ratio of neutrons versus protons decay by β^+-*emission*, also known as positron emission. This process is described in equation 3.1, using ^{18}F as example:

$$^{18}\mathrm{F} \rightarrow {}^{18}\mathrm{O} + \beta^+ + v \tag{3.1}$$

where β^+ is the *positron* and v is a *neutrino*, a small particle without charge and practical mass. The positron particle resembles the more well-known electron, which in this context could be called a *negatron*, having similar mass and an equal but opposite charge of the positron.

Only positron emission is relevant for PET imaging, and several light, positron emitting radionuclides are in clinical use today, such as ^{11}C, ^{13}N, ^{15}O. Most widely used is ^{18}F, which has a relatively long physical half-life of about 110 minutes and decays by positron emission 96.7 % of the times with a mean and maximum energy of 250 and 634 keV, respectively [37]. Another kind of decay seen in radionuclides with relatively few neutrons is *electron capture*, which is responsible for the remaining 3.3 % of the decays. This type of decay can not be used for PET imaging, and is more dominant in heavier atoms, which explains the use of relatively light isotopes for PET. [21]

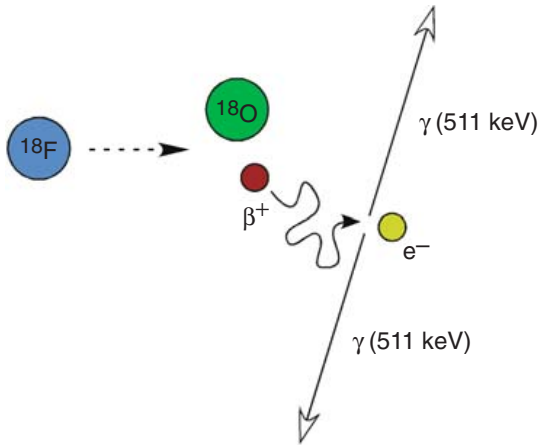

Figure 3.1 – Schematic illustration of positron (β^+) emission from ^{18}F, followed by positron-electron annihilation and emission of two photons (γ). The daughter nucleide is ^{18}O, which is also shown in equation 3.1. From [17].

As opposed to the electron, the positron can not exist freely. After emission, the positron will gradually lose its kinetic energy through a series of inelastic collisions, and finally *annihilate* with a free electron as illustrated in figure 3.1. The distance travelled by the positron depends on the medium, in this case tissue, and the kinetic energy of the positron. As positron emission occurs with a continuous energy distribution, the distance at which the annihilation happens varies accordingly. [43]

In positron-electron annihilation, the two particles unite and their masses are converted into energy emitted as photons. This conversion happens according to the well-known equation 3.2:

$$E = mc^2 \tag{3.2}$$

where E denotes energy, m is the mass and c is the speed of light.

As the mass of the two particles is always the same, so will the dispersed energy be - 2×511 keV. Due to the conservation of momentum and mass, the two photons are emitted almost in direct opposite direction of each other, e.g in 180° angle - this is the key to PET imaging, exploited in *electronic collimation*, which is detailed in section 3.2. The line created by the two photons is called the *Line of Response* (LOR), which refers to the fact that the scanner is only able to detect that the annihilation occurred somewhere on this line, not where exactly.

3.1.1 Tracer compound

In most cases, the radionuclide tracer is contained in a more complex *tracer* molecule, depending on the clinical purpose of the examination. One such compound is *FDG*, formally $2-deoxy-2-(^{18}F)fluoro-D-glucose$, a glucose-analog, only difference is that a hydroxyl group is exchanged with an ^{18}F molecule. As normal glucose, FDG is transported into the cell by transport glucoproteins, commonly known as GLUTs, which is the first process governing FDG distribution. The second process is the phosphorylation by hexokinase, which yields FDG-6-phosphate. The lack of a vacant hydroxyl group in this molecule, compared to normal glucose, traps the analog here until the nuclear decay described by 3.1. As FDG initially follows the pathway of tradional glucose, this makes it an excellent tracer for imaging glucose metabolism, which is elevated in several kinds of neoplastic tissue. [39, 23]

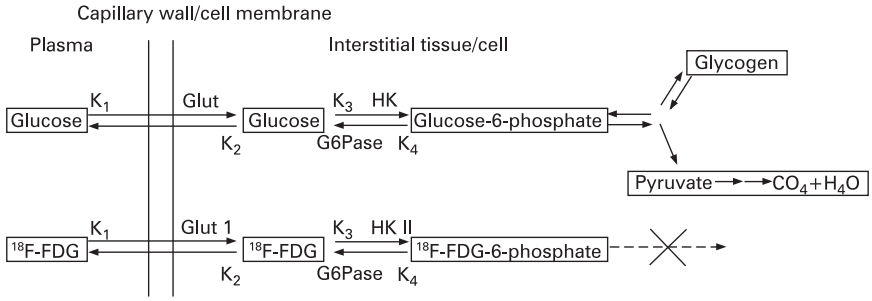

Figure 3.2 – Distribution of normal glucose and FDG. The molecules are identical, except that FDG has an ^{18}F instead of an hydroxyl group. Transport glucoproteins (GLUTs) moves the molecules into the cell, where it is phosphorrylised by hexokinase. From here, FDG can not move further until the ^{18}F has decayed. From [23].

3.1.2 Photon interaction

Just as the positron is eventually annihilated due to loss of energy from interactions with the tissue, so will the 511 keV photons interact with the tissue, however the mechanisms are different. The interaction of photons is described by equation 3.3, which covers both attenuation and scattering:

$$I(x) = I_0 \exp(-\mu x) \tag{3.3}$$

where I denotes the photon flux, x is the distance travelled and μ is the *linear attenuation coefficient*, an estimate of interaction probability. [21, 43]

The amount and kind of interaction depends on the energy of the photons, and at 511 keV, the two primary interactions are *Compton scattering* and *photoelectric absorption*. Detection of the photons eventually relies on the latter, but in the tissue, these interactions

are undesirable as they contribute to noise. Generally, two techniques are applied to correct for these issues:

Scatter correction During compton scattering, the photons change direction, yielding a false LOR as illustrated by the **S** event in figure 3.3. Scatter correction attempts to remove these events, that are detected as *true*, but originates from scattering. In the nature of these events, they can not be distinguished by the scanner. Instead, a statistical model is created from simulations and applied.

Attenuation correction Besides the energy of the photon, the value of μ depends on the atomic number of the medium it transverses, i.e. the density of the tissue. As PET relies on two photons and the LOR they create, the attenuation correction is independent of where on the LOR the annihilation occurred. The attenuation correction is estimated for each LOR from a map of attentuations, often a low-dose CT-scan. This can be said to replenish the events removed by the scatter correction.

In this perspective, a CT-scan builds on the same physical principles, only utilised differently. The CT-scan transmits low energy photons through the body, with contrast generated from different attenuation coefficients; compared to PET, which detect photons originating from within the object, and attenuation is a source of error.

3.2 The device

The modern PET scanner is a complicated machine, that consist of three major parts: detection crystal ring, coincidence electronic circuit and a computer for recording.

3.2.1 Crystal ring

The PET scanner detects the photons from the annihilation radiation by a static ring of scintillation crystals, as shown in figure 3.3. The Siemens TrueGraph PET/CT scanner used in this project is equipped with *lutetium oxyorthosilicate* (LSO) crystals, which are superior by having a very high light output and short dead-time [46, 14, 42].

Every pair of recorded photons is called a *promt*, and as illustrated in figure 3.3, recorded events are divided into three categories:

- **True events (T)** are events that fulfil three requirements:
  - Time between detection is within the *coincidence window*, which is only 4.5 ns on the Siemens TrueGraph scanner due to the LSO crystals [46].

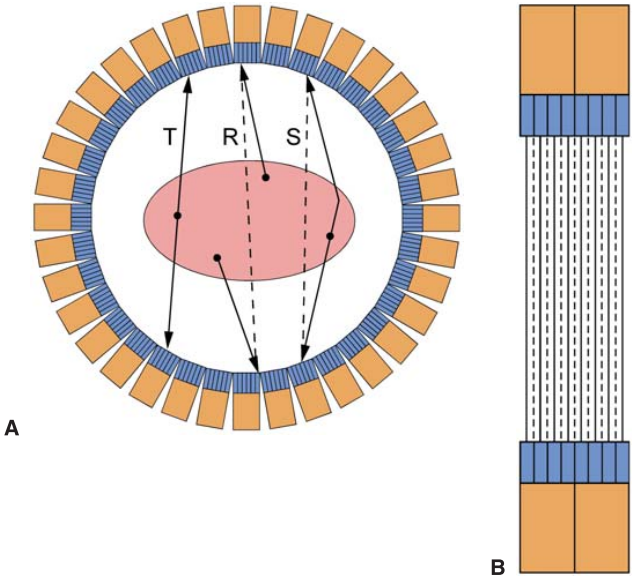

Figure 3.3 – Schematic structure of the detector ring in a modern PET scanner. The scintilation crystals (blue) surround the patient (pink) transaxially. Each group of crystals are coupled with a PMT (yellow) for amplification of the recorded light pulse. **A.** Trans-axial view showing the three kinds of events; trues (T), randoms (R) and scatter (S). **B.** View from the side, showing multiple detector rings. From [17].

  - The energy of the detected photons are within some proximity of 511 keV, usually the window is 350-650 keV [34].
  - The LOR yielded by the two photons are within a meaningful geometric window.

- **Random events (R)** occur when only one of the emitted photons are recorded. This can be due to geometry, attenuation, etc. Random events constitute more than 80% of the recorded events.
- **Scattered events (S)** are seen when one or both photons experience scattering, thereby yielding a false LOR.

3.2.2 Coincidence detection circuit

As the photons hit the crystal, they are converted to a light pulse proportional to the energy of the photon. The pulse is amplified and converted into an electrical signal by one or more *Photo Multiplier Tubes* (PMT), as seen in the top part of figure 3.4.

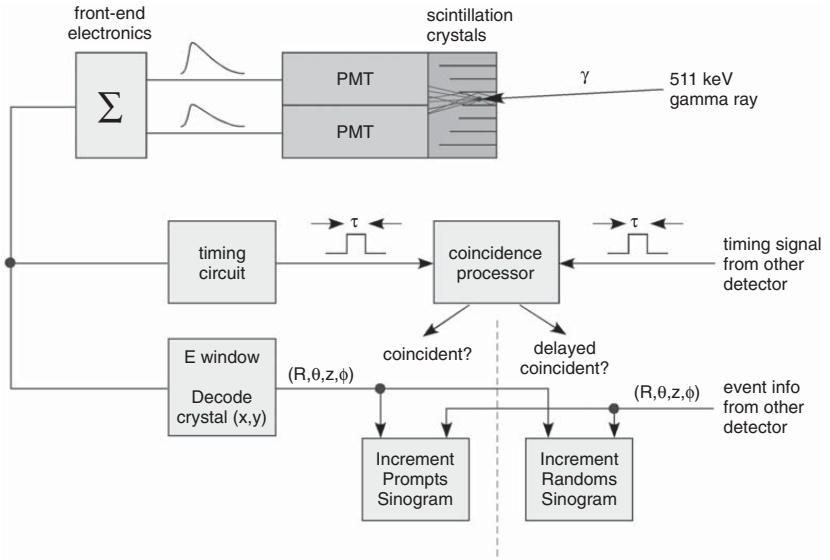

Figure 3.4 – Overview of PET detection circuit, which starts with the detection of a photon, γ, in the top right corner. It is converted to an electrical pulse by the PMT, which is transmitted to the coincidence circuit, determining if it is a true event. The prompt is then recorded in the corresponding sinogram or in list-mode (not illustrated). From [17].

The electrical pulse from the PMT is then passed through the coincidence detection circuit. Due to the nature of the annihilation, a recorded pulse should match with another pulse from another detector within coincidence window, τ. The size of this window should be wide enough to catch all true events, but as narrow as possible to reduce the number of scattered events. For LSO crystals, having a relatively good temporal resolution, it can be as narrow as 3-5 nanoseconds [42].

3.2.3 Data recording

After having defined its type, the event is stored in a computer. Traditionally, the events are histogrammed into *sinograms*, which are pre-defined matrices where each element represent a pair of detectors. Before the scan, the numbers and duration of each sinogram, corresponding to one frame, are chosen.

With recent improvement in computer hardware technology, such as memory and bandwidth, so-called *list-mode recording* have become available, which are used in the present study. Instead of collecting the data directly into sinograms, every single event is recorded and stored for later histogramming, which yields complete freedom to do whatever recon-

structions are wanted at a later time point. This is illustrated in figure 3.5.

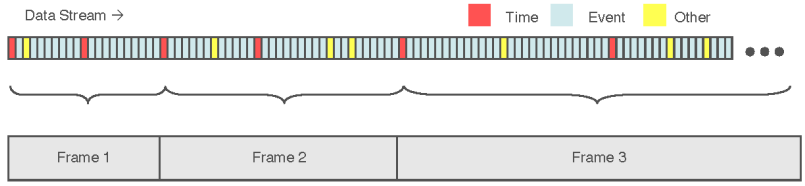

Figure 3.5 – Illustration of listmode recording. The list is illustrated as blocks, most of them being promts, each registered with the corresponding crystals. Time stamps are put in the list too, along with other relevant information. The data can then be histogrammed into sinograms in any way desired later on. From [7].

4

Imaging and statistics

This section presents some of the mathematical theory used in the project, such as various algorithms for tomographic image reconstruction, image transformation and statistical analysis. A brief review of some relevant previous studies is also included, as well as an introduction to cardiac magnetic resonance imaging, which is used for validation.

4.1 Image reconstruction

Despite the relatively short history of tomographic imaging, several algorithms for reconstruction of images have been developed. They are generally divided into analytical and iterative algorithms.

4.1.1 Analytical techniques

The algebraic reconstruction algorithm *filtered back projection* (FBP) was the first method applied to reconstructing tomographic data, as used by [29]. It has been the work-horse for tomographic imaging due to computational speed and stability.

The sinogram, described in section 3.2.3, can be interpreted as a number of projections of an 2D object onto a 1D space at a given number of angles. Mathematically, this is described by the Radon transform ($\mathcal{R}$), which is given as:

$$\begin{aligned} p_\phi(x') &\equiv \mathcal{R}[f(x,y)] \\ &= \int_{-\infty}^{\infty} f(x'\cos\phi - y'\sin\phi, x'\sin\phi + y'\cos\phi)\, dy' \end{aligned} \tag{4.1}$$

where $p_\phi(x')$ denotes the projection data at a given angle ϕ, f is the object being imaged and x' is the coordinate in the new space.

The reconstruction is facilitated by an important relation between the one-dimensional Fourier transform of a projection and the two-dimensional Fourier transform of the image. This theorem is known as the *Central Slice Theorem* or the *Fourier Slice Theorem*:

At first, the one dimensional Fourier transform of a projection is considered:

$$\begin{aligned} P_\phi(\omega) &\equiv \mathcal{F}_1\left[p_\phi(x')\right] \qquad (4.2)\\ &= \int_{-\infty}^{\infty} p_\phi(x')\, e^{-j\omega x'}\, dx' \\ &= \int\int_{-\infty}^{\infty} f(x'\cos\phi - y'\sin\phi, x'\sin\phi + y'\cos\phi)\, e^{-j\omega x'}\, dx'\, dy' \qquad (4.3)\end{aligned}$$

where (4.1) is used in the last step. By changing coordinates, (4.3) is rewritten into (4.4), which leads to the two-dimensional Fourier transform of the object:

$$\begin{aligned} P_\phi(\omega) &= \int\int_{-\infty}^{\infty} f(x,y)\, e^{-j\omega(x\cos\phi + y\sin\phi)}\, dx\, dy \\ &= F(\omega\cos\phi, \omega\sin\phi) \qquad (4.4)\\ &= F(\omega,\phi)\end{aligned}$$

To summarize, the central slice theorem relates the one-dimensional Fourier transform of the projection data to the two-dimensional Fourier transform of the image in polar coordinates. The estimated image, $\hat{f}(x,y)$, can be found from the inverse, two-dimensional Fourier transform of the frequency data, $F(\omega_x, \omega_y)$.

$$\hat{f}(x,y) = \int_{-\infty}^{\infty}\int_{-\infty}^{\infty} F(\omega_x,\omega_y)\, e^{j(x\omega_x + y\omega_y)} d\omega_x\, d\omega_y \qquad (4.5)$$

In order to apply the central slice theorem, (4.5) is converted to polar coordinates (4.6). When doing so, the Jacobian should be added, which is found to be $|\omega|$. This parameter is essentially a spatial filter, and can be modified in order to obtain some compromise between smoothing and sharpness in the image [8].

$$\hat{f}(x,y) = \int_0^{\pi}\int_0^{\infty} F(\omega,\phi)\, e^{j\omega(x\cos\phi + y\sin\phi)} |\omega|\, d\omega\, d\phi \qquad (4.6)$$

where the limits of integration is changed, so $0 \le \phi < \pi$, as this is sufficient for reconstructing the entire image. Using the central slice theorem from (4.4), $F(\omega,\phi)$ is substituted with $P_\phi(\omega)$, and the two integrals are split up:

$$\begin{aligned} \hat{f}(x,y) &= \int_0^{\pi}\left[\int_0^{\infty} |\omega| P_\phi(\omega)\, e^{j\omega x'}\, d\omega\right] d\phi \\ &= \int_0^{\pi} p^*_\phi(x') d\phi \qquad (4.7)\end{aligned}$$

where

$$p_\phi^*(x') = \int_0^\infty |\omega| P_\phi(\omega)\, e^{j\omega x'}\, d\omega$$
$$= \mathcal{F}^{-1}\left[|\omega|\, P_\phi(\omega)\right] \tag{4.8}$$

This derivation is for two dimensional data, but can be conceptually transferred to three dimensions.

4.1.2 Iterative techniques

In 1994, [30] presented the *Ordered Subset Expectation Maximization* (OSEM) algorithm, an accelerated version of the general maximum likelihood algorithm, specifically developed for SPECT and PET. General iterative algorithms had been proposed earlier, but the division of computations into subsets made the processing time for reconstructions reach an acceptable level.

The iterative process is somewhat opposite of the analytical, and starts out with an initial guess of the object, $f^*(x, y)$, then simulates the projection and compares with the obtained sinogram, as illustrated in figure 4.1, and the initial guess is updated. This is described by equation 4.9:

$$f_i^{k+1} = \frac{f_i^k}{\sum_j M_{i,j}} \sum_j \frac{M_{i,j}\, s_j}{\sum_i M_{i,j}\, f_i^k} \tag{4.9}$$

where f is the image, s denotes the projection data and M is the cost matrix. k is the current iteration, and i and j denotes indexes of image and projection data, respectively.

OSEM models each pixel as a Poisson process, thereby improving the model over the line integral of the analytical FBP. The modelling can be refined further, as with the Siemens TrueX algorithm, which incorporates a scanner-specific point spread function (PSF) model to each voxel. The iterative techniques are generally more computationally demanding, as each iteration corresponds to a single analytical solution, but also potentially offers better SNR and spatial resolution. For most clinical reconstructions, TrueX is the primary choice.

4.2 Image processing

The basic linear transformation is called an *affine* transformaion, and allows for translation, rotation and anisotropic scaling of data. The transformation can be described as

$$\mathbf{y}(\mathbf{x}; \mathbf{A}, \mathbf{t}) = \mathbf{A}\mathbf{x} + \mathbf{t} \tag{4.10}$$

with $\mathbf{x}$ and $\mathbf{y}$ denoting the input and transformed data, respectively. $\mathbf{A}$ is an N-by-N matrix that describes scaling and rotation for the N-dimensional data, and t yields the translation.

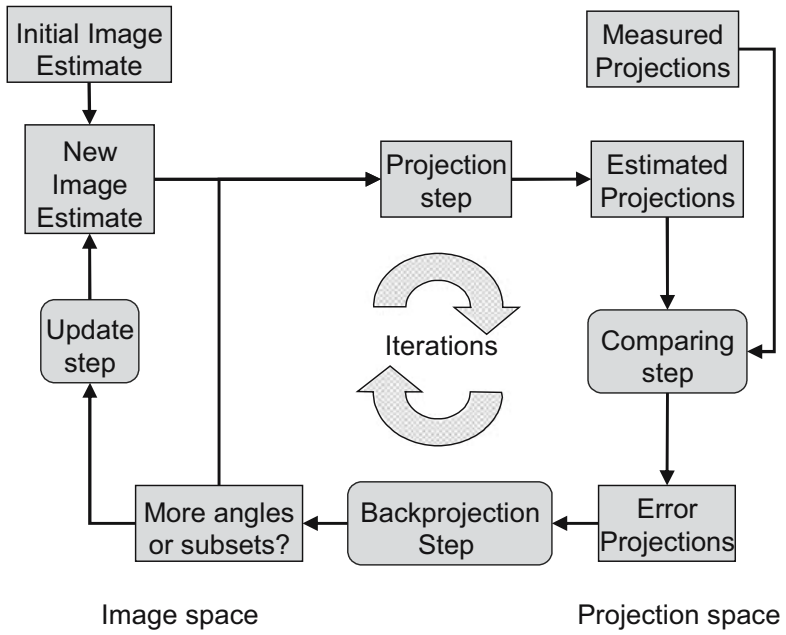

Figure 4.1 – Schematic presentation of the iterative reconstruction algorithms. As opposed to the analytical algorithm, the estimate of the image is projected forward into a sinogram, that is then compared to the sinogram obtained by PET. From [24].

As described in chapter 2, the only operation required for cardiac images is rotation. Hence, the matrix $\mathbf{A}$ is replace with the Euler rotation matrix, $\mathbf{R}$, an 3×3 matrix defined as

$$\mathbf{R} = \begin{pmatrix} 1 & 0 & 0 \\ 0 & \cos\theta_1 & \sin\theta_1 \\ 0 & -\sin\theta_1 & \cos\theta_1 \end{pmatrix} \begin{pmatrix} \cos\theta_2 & 0 & -\sin\theta_2 \\ 0 & 1 & 0 \\ \sin\theta_2 & 0 & \cos\theta_2 \end{pmatrix} \begin{pmatrix} \cos\theta_3 & \sin\theta_3 & 0 \\ -\sin\theta_3 & \cos\theta_3 & 0 \\ 0 & 0 & 1 \end{pmatrix}$$

where θ_1, θ_2 and θ_3 represent the angles of rotation around the coordinate axes.

4.3 Statistics

4.3.1 Nyquist-Shannon sampling theorem

Several mathematicians formulated the *sampling theorem* independently and in different ways during the first half of the 20th century. Most often, the formulation is credited Nyquist and Shannon, who originally stated:

Theorem 4.1 *If a function $f(t)$ contains no frequencies higher than W cps, it is completely determined by giving its ordinates at a series of points spaced $1/2W$ seconds apart.* [45]

A more general and modern phrasing would be that any signal should be sampled at minimum twice the rate as the highest frequency component of the signal. Applying this in an pertinent example; the temporal resolution of images of the heart should be twice that of the heart rate in order to represent the contraction adequately. This is illustrated in figure 4.2, where the black curve is the actual signal. The red dots represent the sampling points, and the dotted red line is the false signal obtained by under-sampling.

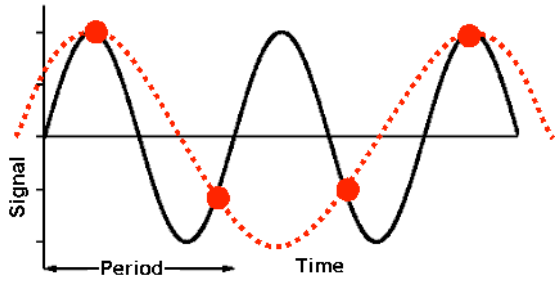

Figure 4.2 – Illustration of the Nyquist-Shannon sampling theorem. The black curve represents the actual signal, and the red dotted curve is the false result of under-sampling at the bold points. From [50].

4.3.2 Poisson distribution

As described in chapter 3, the promts recorded in PET are events, and hence distributed according to the Poisson distribution, given by equation 4.11. The Poisson distribution is unique because both the expected value, i.e. the mean, and the variance is given by the intensity parameter λ. This implies that the reconstruction algorithms should account for a higher variation when the number of events are high.

$$f(x;\lambda) = \frac{\lambda^x e^{-\lambda}}{x!} \tag{4.11}$$

where λ is the intensity parameter. Furthermore, the mean and variance is given as

$$E(X) = \lambda \qquad (4.12) \qquad\qquad Var(X) = \lambda \qquad (4.13)$$

4.3.3 Gamma-variate

The input function for the tracer in the heart is often modelled by a Gamma variate function [15], as described in equation 4.14. This is closely related to the Gamma distribution, which is very general and is seen often in biomedical analysis.

$$f(x;\alpha,\beta) = \frac{x^{\alpha-1}e^{-x/\beta}}{\beta^{\alpha}\Gamma(\alpha)} \quad , \; x,\alpha,\beta > 0 \qquad (4.14)$$

where α and β are parameters, and $\Gamma(\alpha)$ denotes the *gamma function*, given by

$$\Gamma(\alpha) = \int_0^{\infty} x^{\alpha-1}e^{-x}\,dx \;\Rightarrow\; (\alpha-1)! \text{ for } \alpha \in \mathbb{N} \qquad (4.15)$$

4.3.4 Analysis of variance

The *analysis of variance* (ANOVA) is a statistical framework for estimating which effects account for variation in a dataset. Effects can be *fixed* or *random*: Fixed effects allow for certain assumptions, which simplifies the analysis, but the analysis is only valid for the chosen treatments. Using random effects, the treatments are considered sampled randomly from a larger population. [35]

The present project uses a *mixed model*, where the number of bins and reconstruction methods are considered fixed factors, but where patients are included as a random factor. This is formulated is equation 4.16:

$$y_{ijkl} = \mu + \alpha_i + \tau_j + \alpha\tau_{ij} + \rho_k + \varepsilon_{ijkl} \qquad (4.16)$$

where α denotes the effect of bin size, τ denotes the reconstruction algorithm effect, ρ is the patient effect and ε is the estimation error.

4.4 Previous work

This section presents and elaborates on some of the previous work done in the field of first-pass estimation of cardiac ejection fraction, with a focus on using PET imaging.

As described in section 1, several modalities compete in the field of estimating RVV, each with their strength and weaknesses. The variety of methods available might have limited the desire for examining PET further for this purpose, as there are quite many papers comparing the different modalities in RVV estimation.

4.4.1 Early work

Some of the first to present the basic concept of first-pass was Mullani and Gould [36], with the idea of a mathematical kinetic first-pass flow model. The principle is rather simple; the concentration of a uniformly distributed tracer in a volume can be described as the difference between the integral of the flow to and from the volume, respectively. Initially, there is no flow out of the volume, and measurements for the flow towards the organ can be made. However, the focus in the work is on distribution of the tracer in the cardiac muscle tissue, the myocardial perfusion, and not a blood pool study as the present project.

Much of the previous work has been done in combination with myocardial perfusion examinations, such as Chen et al. [10]. The focus is on the left ventricular output and kinetic models are used. During a traditional examination of myocardial perfusion, temporal sampling of 0.2 Hz was made during infusion of tracer, and a time-activity curve was constructed for a ROI in the left ventricle and fitted to a gamma-variate function.

4.4.2 Animal studies

Several interesting animal studies have been published. The use of small animal PET-scanners with research software and possibility to administer higher doses, hence achieving better count statistics, makes it easier to do higher temporal sampling. Several papers by a group at David Geffen School of Medicine at UCLA, USA, present high temporal sampling PET imaging for cardiac output estimation [54, 32, 19]. Despite a frame rate of only 0.3 s, the work still rely on kinetic models or other assumptions, due to the very high heart rate of mice, which is about 300 bpm.

4.5 Cardiac Magnetic Resonance Imaging (cMRI)

Nuclear Magnetic Resonance (NMR) is not a member of the nuclear medicine family, despite its name. It was originally designed as a technique for spectroscopic analysis of molecules, but is widely used for human imaging today, and so commonly known as magnetic resonance imaging. Instead of ionizing radiation, the modality relies on strong magnetic fields and radio waves, and employs a quantum mechanic nucleus property, *spin*, which yields the nuclei with a magnetic moment. Most clinical imaging uses hydrogen nuclei in water, ^{1}H, which is abundant in the human body and is sensitive to perturbation by RF-pulses, as it has a relatively large *gyromagnetic ratio* (γ). This quantity is a part of the *Larmor equation* given by equation 4.17, which is one of the most fundamental equations of MRI.

$$\omega_0 = \gamma \, \mathrm{B}_0 \tag{4.17}$$

where ω_0 is the precession frequency of the nuclei, γ is the gyromagnetic ratio and B_0 is the applied magnetic field strength.

By applying a powerful magnetic field, about ten orders of magnitude stronger than earth's own, a slight alignment of the magnetic moments are achieved. By applying RF-pulses at the *resonance frequency*, the magnetic moment can be turned, and a signal obtained when it returns towards equilibrium. Adjustable gradients are placed in the magnetic field, which encodes spatial information. Images can then be made of any plane in the body. Furthermore, RF-pulse can be applied in numerous ways, called a *sequence*, making MRI an exceptionally versatile technique. As with most nuclear medicine modalities, cMRI is recorded along with an ECG for adjusting to the cardiac cycle. In connection with cMRI, this time-resolved method is often referred to as *cine* MRI.

As opposed to PET, which yields quantitative estimates of tracer distribution, MRI is based on contrast imaging for anatomical studies, hence the absolute signal amplitude has little meaning. Two approaches for assessing cardiac viability are taken in cMRI: For estimates regarding left ventricle, most clinical routines rely on geometric assumptions, such as those shown in figure 4.3a. Even the simple geometric models give good estimates due to the rather straightforward anatomy of the left ventricle, but this is not the case for the right ventricle, as described in section 2. For reliable estimates, full volume quantification must be made, as illustrated in figure 4.3b. Each slice of the heart is contoured, and the volume is found by summation of the slices. In a study of 52 healthy volunteers, Rominger et al. [44] reported an average RVEF of $61.6 \pm 6.3\%$ using cMRI. As a comparison, Pfisterer et al. [40] reported a general normal value range of $52.3 \pm 6.2\%$ using nuclear medicine (N=365).

Previous sequences used in cMRI relied on the blood flow, where signal from stationary tissue was saturated, while the newly arrived blood could yield a stronger signal. This produced a clear contrast, and became known as bright-blood sequences. The sequences currently used in cMRI are balanced gradient-echo sequences. These methods were introduced already in the 1980s, but were not useful until recent hardware improvements, such as a higher degree of homogeneity of the magnetic field. The sequences are balanced in the way that they perturb the signal in a steady-state manner, such that the recorded

signal is fairly constant. The result is a very fast sequence, about 1 second for each slice, with a superior liquid to tissue contrast.

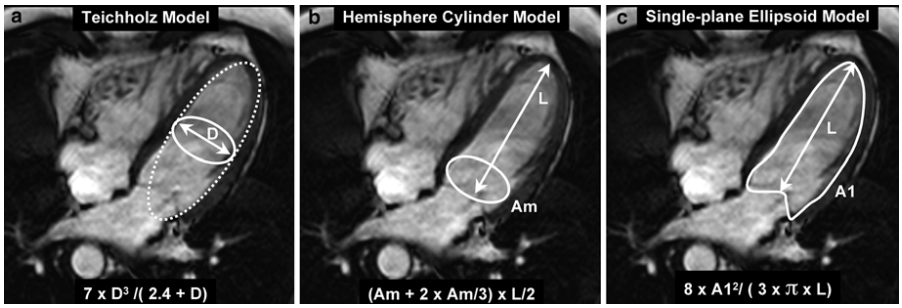

(a) Three different geometric assumptions for estimating LV volume, with the corresponding formula in the bottom of each image. **a** Teichholz method, **b** Hemisphere cylinder method and **c** Single-plane ellipsoid method.

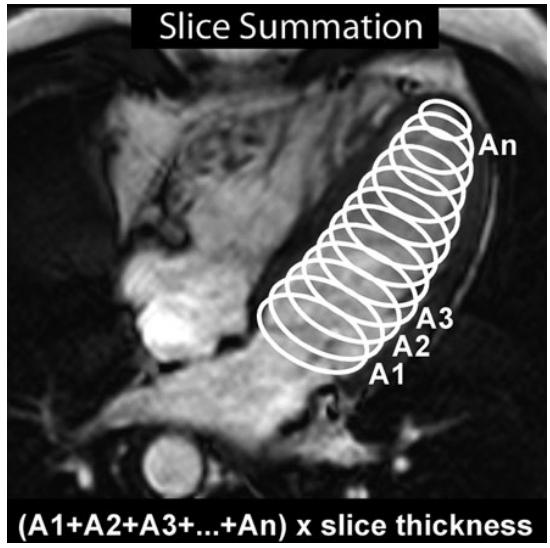

(b) Volume quantification by slices. An ROI is drawn for each slices, and volume is estimated by summing these.

Figure 4.3 – Illustrations of methods for estimating ventricular size and function from anatomical cMRI. From [5].

5

Data

This project is based on data from a larger clinical study conducted at Rigshospitalet and Frederiksberg Hospital by MD, PhD Henrik Gutte and professor, MD, PhD, DMSc Andreas Kjær. It was conducted as a part of a PhD study with the motive of investigating the significance of different clinical tools for diagnosis of right ventricular inadequacy as an indicator of pulmonary embolisms [22]. By comparing the significance of biochemical markers and cardiac nuclear medicine, the project aimed to make diagnosis of right ventricular dysfunction easier and more reliable.

Part of the study was an idea of expanding the well-established concept of first-pass RNV to the PET modality. Initially, the feasibility of the technique was investigated in an animal study on rats [12], using MicroPET (Focus 220, Siemens Preclinical Solutions). Being a preliminary study, only one rat was scanned, and the RVEF was estimated to be about $25 \pm 5\%$, which is considerably lower than expected. However, the animal study faced several challenges, similar to those described in section 4.4, such as the small heart and high heart rate of about 300 bpm in the rat, which introduced considerable uncertainties.

The clinical study on human patients was initiated and performed, however, technical issues in the image analysis delayed this part to a degree that it was excluded in the final report. These challenges, as described in section 1.2, are addressed in the present thesis. One of the practical challenges was to obtain the required temporal sampling, as described in section 4.3.1. The Siemens TrueGraph reconstruction software is capable of performing dynamic reconstructions from list-mode data, but with a minimum of 1 second frame duration, corresponding to 1 Hz temporal sampling.

5.1 Data set

23 patients who were referred to the Department of Clinical Physiology, Nuclear Medicine and PET at Rigshospitalet for a FDG-PET scan, were recruited to participate in the study

during the period of October 2008 till June 2009. 21 of these patients [13 female, 8 males, mean age 51.4 ± 12 years] had a FDG-PET scan according to the protocol described in section 5.2 and 15 underwent cMRI scan for RVEF estimation according to clinical procedure. That leaves 13 patients who had both scans, and this data is used to examine correlation between the RVEF values estimated in this project and those of the MRI scan.

The FDG-PET scan was performed on a Siemens TrueGraph40 scanner at Rigshospitalet, Copenhagen, Denmark by trained technicians and with a physician present. The scanner is equipped with 192 detector blocks, each containing 169 LSO crystals with 4 attached PMTs. This enables for a theoretical isotropic resolution of just over 2 mm.

5.2 Experimental PET protocol

The PET examination is divided into three parts:

1. 5 minutes dynamic list-mode recording during bolus injection (defined at time = 0).
   - Patient is prepared as for a routine FDG-PET exam, with venous catheter in the elbow joint, but without injection of FDG. Three electrodes are placed on the patient chest for ECG recording.
   - A 25 cm topogram is recorded, and the FOV is set over the heart according to this.
   - A low-dose CT scan of the heart is performed for attenuation correction.
   - The patient bed is then moved to the PET position, while the FDG is prepared. Approximately 425 MBq of FDG is dissolved in a 0.9 % NaCl solution to a total volume of 1 ml.
   - The scanner is set for 5 minutes of list-mode recording, and 5 seconds after start, the FDG is injected as a bolus along with 20 ml of standard NaCl solution.
2. 15 minutes dynamic list-mode recording started 40 minutes after the FDG bolus is injected. At this point, FDG is distributed, primarily to the myocardium.
   - After the primary 5 minute first-pass scan, the injection tubes are removed, the patient bed is moved out of the scanner, and the patient rests here for about 35 minutes.
   - When the FDG is distributed in the myocardial tissue, the patient bed is moved back into the scanner. A standard cardiac CT scan is performed, followed by a 15 minutes PET list-mode recording.
3. From here on, the normal procedure for FDG-PET scan is followed, as requested by the referring physician.

5.3 MRI validation protocol

The patients were referred to a cMRI scan at Frederiksberg Hospital, where both left and right ventricular viability was estimated, including EF, according to normal clinical protocol. The scans were performed on a Phillips Intera 1.5T scanner using a phased array coil, specifically designed for cardiac imaging (Synergy). The sequence used was a *Balanced Turbo Field Echo* (b-TFE), a balanced gradient-echo sequence, as described in section 4.5. It had a repetition time (TR) of 3.2 ms, an echo time (TE) of 1.6 ms and a 60° flip angle.

After an initial localisation of the heart, 12 slices of 10 mm were obtained in short-axis view. Scan time was 65 to 85 seconds, with breath-holding and ECG-gating applied. The cardiac cycle was divided into 30 phases, and the FOV was 320 mm. After the scan, endomyocardial ROIs were drawn manually on each slice in each phase, and volumes were then estimated by summing slices, as illustrated in figure 4.3b.

An example of the analysis is shown in figure 5.1, and all the obtained values are listed in table 7.1.

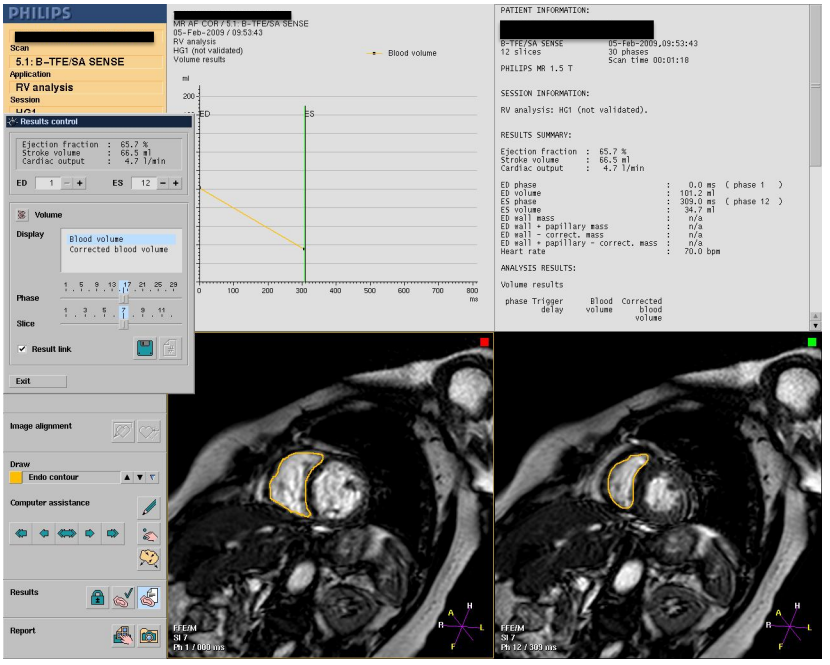

Figure 5.1 – Example of RVEF estimation by MRI. Scan was performed using a b-TFE sequence as described in the main text. The right ventricular volume of each slice and phase was drawn by hand, and calculated by summation.

6

Estimation of RVEF

6.1 Initial considerations

As stated in section 1.2, several challenges in estimating RVEF using first-pass FDG-PET were clear from the beginning. Besides the need for fast temporal sampling and short time window available, it quickly became clear that the need for drawing a precise *Region of Interest* (ROI) was essential. The ejection fraction is a ratio as stated by equation 1.1, so if the atrium is included in the calculations, this would yield a lower EF than expected.

The first issue to be addressed was the temporal sampling. As the scanner workstation did not allow for shorter frames than 1 second, an alternative approach was needed. Two ideas were considered:

6.1.1 List-mode approach

The list-mode recordings have a time stamp for each millisecond, so in theory, it should be possible to do the histogramming into sinograms at shorter time frames than possible on the clinical workstation. However, the structure of the list-mode file as well as the internal algorithms of the scanner workstation are proprietary information, so no documentation of either is available. Through various detours, a script written in `C++` for histogramming the listmode file was obtained. This software is based on the same code used in the scanner workstation, but allows for bins shorter than 1 second. For each frame, the script would output a sinogram in a format known as *interfile*, created by Department of Medical Physics and Bioengineering, University College, London, UK [52]. Unfortunately, the format is not defined very well, and implementations vary greatly.

Several attempts were made to convert the sinograms made this way into a format readable by the scanner workstation, without success thought. The de facto standard for medical

images today is the *Digital Imaging and Communications in Medicine* (DICOM) standard, which is a complex format capable of storing both image data and meta data. Using the PMOD software package (version 3.304, PMOD Technologies Ltd, Zurich, Switzerland), an attempt was made to convert the interfile sinogram into DICOM format, which is readable by the scanner workstation.

The DICOM metadata is divided into so-called *tags*, which can be private or open. The Siemens workstation requires a series of private tags in order to accept the file, preventing the converted file from being accepted by the scanner workstation. As these private tags are presumably put in to prevent doing exactly what is desired here, moving further with this solution would require a partnership with Siemens in order to get technical, proprietary information. Performing the entire reconstruction outside the clinical workstation environment would require information on the geometry etc.

6.1.2 ECG-gating approach

Another solution was to use ECG-gated reconstruction, which is already used in a variety of cardiac studies. The assumption is that each cardiac cycle is identical, hence each phase can be summed across heart beats. The ECG recorded during scan is analysed and the time between R-peaks are divided into a user defined number of bins, each which is then summarised over cardiac cycles. This utilisation of the periodic nature of the cardiac cycle yields a number of frames, each representing a part of the cardiac cycle, as illustrated in figure 6.1.

The input function of the heart is modelled as a gamma-variate function, as described in section 4.3.3. Simultaneously, the heart is pumping, making the amount of tracer in the heart fluctuate. This is illustrated in figure 6.2a, where the thick vertical lines indicate the relevant time window. The dotted vertical lines illustrate the individual cardiac cycles, which are then each divided as shown in figure 6.1.

6.2 Image reconstruction

As described in section 5.2, two list-mode recordings are made for each patient. These files, along with normalisation information and corresponding CT-scan for attenuation correction was loaded into the scanner workstation from an external hard drive. From this, a number of different reconstructions were made in three steps, described below.

1. Two static reconstructions were made of the entire list-mode files, which are 5 minutes and 15 minutes, respectively. The 5 minute scan primarily show the blood pool, and is intended for ROI drawing for the right ventricle. The 15 minute scan, initiated 40 minutes after injection of FDG, shows the myocardium of the left ventricle clearly, and is used for rotating the image to short-axis view, as described in section

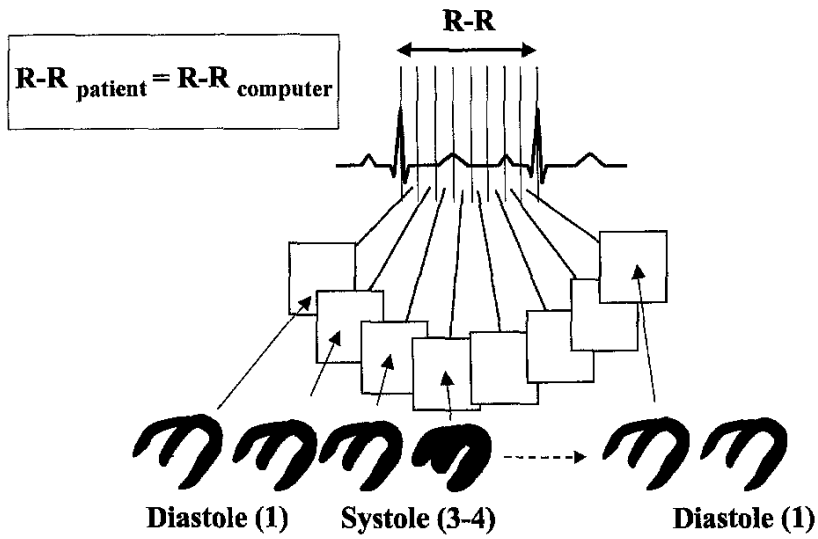

Figure 6.1 – Illustration of cardiac gating using ECG. Each interval between R-peaks are divided into a number of bins, and events from each bin are then summed with the corresponding bins from other cycles. From [13].

4.2. As these reconstructions are for initial analysis, FBP reconstruction is used due to speed.

2. In order to estimate the bolus' way through the heart, that is, the time between bolus arrival at the right ventricle, and the arrival at the left, the first 20 seconds of list-mode data was reconstructed in 1 second frames, e.g. 20 $\times$ 1 second. From this reconstruction, a *Time-Activity Curve* (TAC) was constructed and analysed, an example is shown in figure 6.2b. This gives an estimate of the bolus passage through the heart, and the relevant period for gated reconstruction is chosen. The arrival and passage-time varied from patient to patient. The general criterion was to choose 4-6 seconds just after the peak, such that no activity had reached the left side of the heart.

3. As the relevant passage period is found, a series of gated reconstructions are made. For 8, 12 and 16 bins, and 4 different reconstruction methods (FBP, OSEM2D, OSEM3D and TRUEX), a total of 12 reconstructions are made and exported in DICOM format to an external hard drive. Each of these reconstruction yield a number of 3D images corresponding to the number of bins, and from these an estimate of the RVEF is found, as described in section 6.3.

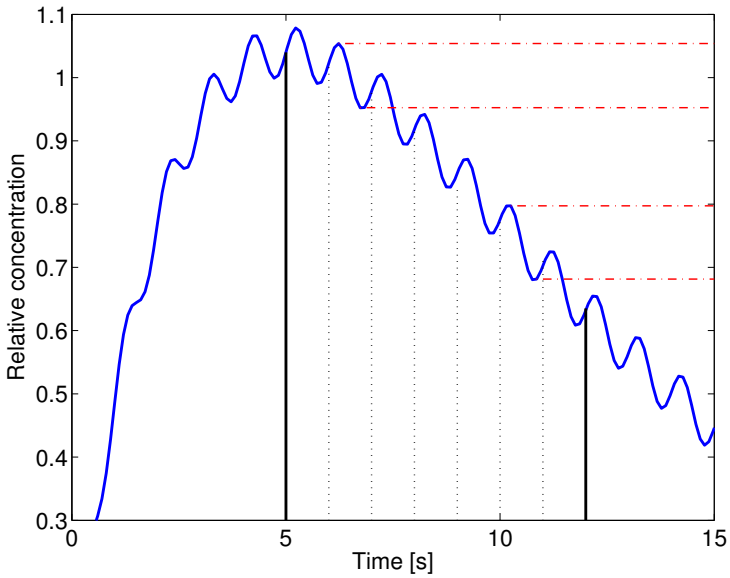

(a) Sketch of idea and assumptions made in the ECG-gating approach. The period delimited by the bold black lines are reconstructed in a gated manner, summing the cycles marked by dotted black lines. The assumption is then that the ratio in each cycle is relatively constant, as illustrated by the dotted red lines.

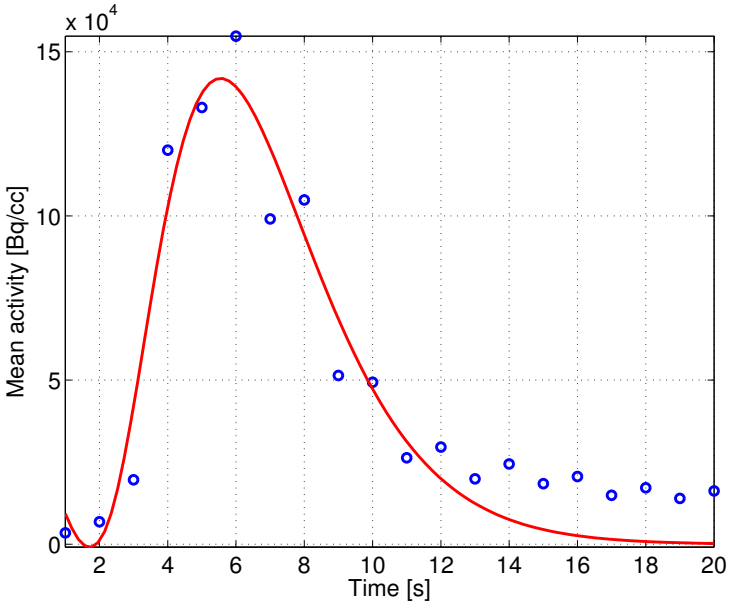

(b) Practical time-activity curve (blue) from patient 19, fitted with a gamma-variate function (red). The fit captures the bolus passage, but not the periodic contractions of the heart.

Figure 6.2 – Time-activity curves. 6.2a Theoretical, 6.2b Practical.

6.3 Image processing

Once an overview over the bolus passage and the main reconstructions have been obtained, the actual estimation process can begin. All image processing was done using MATLAB (version 7.13, The Mathworks, Inc., United States) on an Apple MacBook Pro with an Intel Core2Duo 2.2 GHz CPU and 4 GB DDR2 RAM. Efforts have been put into using existing toolboxes, and all scripts are provided in appendix A.

6.3.1 Reading DICOM files

Each reconstruction is exported from the scanner workstation onto an external hard drive in DICOM format. Most reconstructions were made in $336 \times 336 \times 111$ pixels, and each slice is exported into a separate DICOM file. The MATLAB-script `dicom2mat` loads the individual DICOM files into MATLAB and gathers them in a single variable for each image frame. For the gated reconstructions, one 3D image is created for each bin, yielding up to 1776 DICOM files for one 16 bin reconstruction.

The FOV covers the entire thorax, so as the DICOM files are loaded into MATLAB structure, the image is cropped to $128 \times 128 \times 111$ pixels in order to reduce size.

6.3.2 Image reorientation

Initially, three relevant slices from the 15 minute static reconstruction are shown, one from each plane, as shown in figure 6.3. In each image, the long axis of the left ventricle is identified, and drawn by two points connected by a line. From the two coordinates, the rotation angle is computed using simple geometry and applied to a rotation matrix as described in section 4.2.

The rotation is computed using `com_rot.m`, and applied using `rot2sa.m`, which are both listed in Appendix A.

6.3.3 ROI drawing

After the reorientation, the 15 minute reconstruction is inspected in short axis view to approximately locate the slices containing the apex and atrioventricular septum. While the apex is fairly easy to identify on most of the patients, the atrioventricular septum is considerably harder. A common definition is to use the slice at which the circle created by the left ventricle myocardium in short axis view is about 2/3 complete. An example is shown in figure 6.3b.

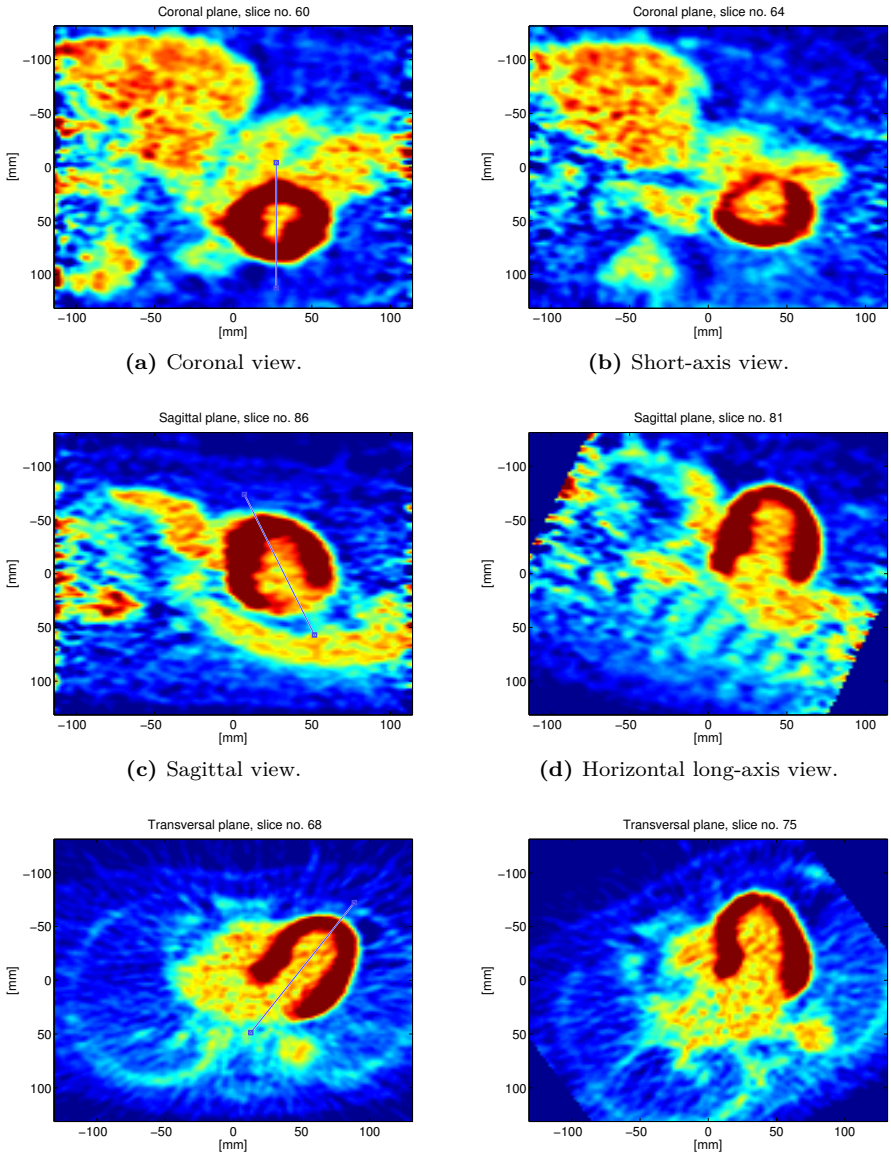

(a) Coronal view. **(b)** Short-axis view.

(c) Sagittal view. **(d)** Horizontal long-axis view.

(e) Transaxial view. **(f)** Vertical long-axis view.

Figure 6.3 – Illustration of the reorientation process, shown for patient number 6. Lines are drawn in 6.3a, 6.3c and 6.3e, and from them, rotation is computed. Figure 6.3b, 6.3d and 6.3f are the rotated versions, shown according to [9].

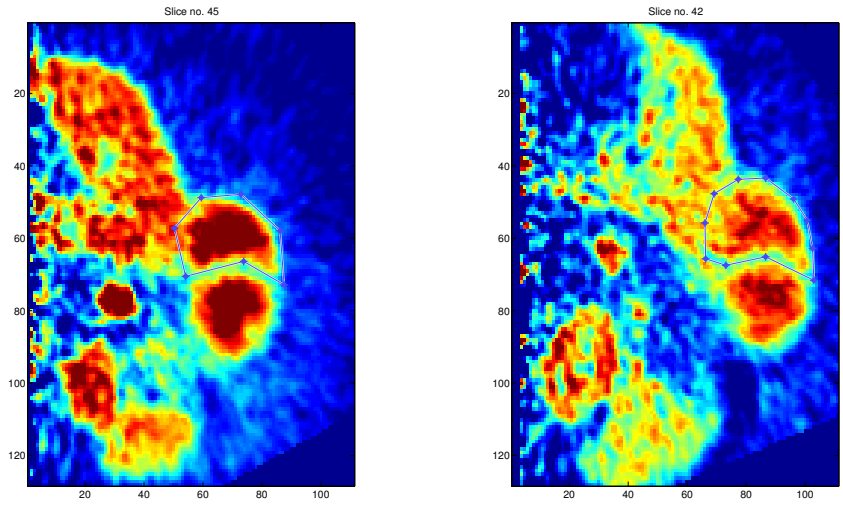

(a) ROI-drawing on patient 19.

(b) ROI-drawing on patient 11.

Figure 6.4 – Examples of ROI-drawing of the right ventricle. The images are in short-axis view, from the first 5 minutes reconstruction, which clearly show the blood pool.

As the slices covering the right ventricle has been identified, the ROI is drawn slice by slice using the 5 minute reconstruction. Here, the blood pool can be identified clearly; two examples of ROI drawing is shown in figure 6.4. All ROIs were drawn by the author for each patient twice, in a manner as consistent as possible. The ROI is then output as a logic matrix of the same size as the image.

6.3.4 Batch processing

The actual RVEF estimation is done in a batch script, where each reconstruction is loaded using `dicom2mat`, rotated using `com_rot.m`, and then summed for each bin using the ROI. For each reconstruction, this yields an volume-curve similar to the one seen in figure 2.5. The obtained curves for patient 9 are shown in figure 6.5. The maximum values are then interpreted as EDV, the minimum as ESV, and the RVEF is estimated according to equation 1.1. The final results are shown in table 7.1.

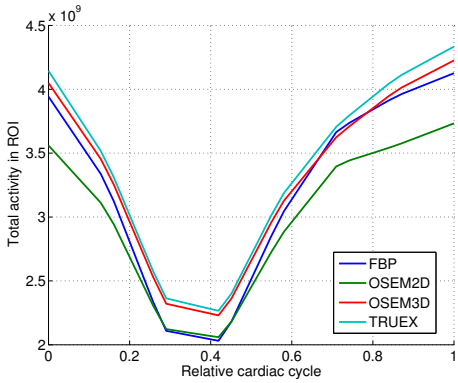

(a) Estimated volume-curves using 8 bins.

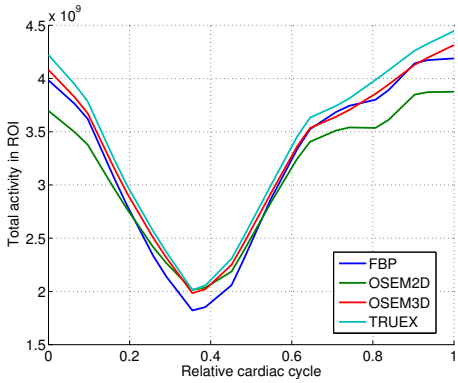

(b) Estimated volume-curves using 12 bins.

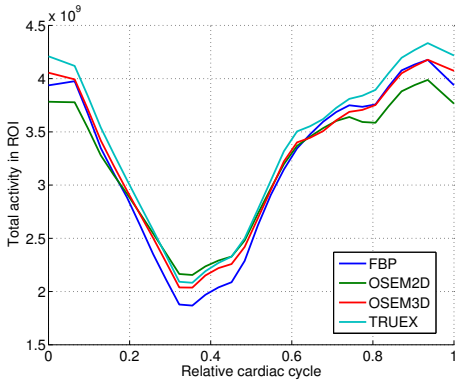

(c) Estimated volume-curves using 16 bins.

Figure 6.5 – Estimated volume of the right ventricle during cardiac cycle for patient 9. The RVEF can be determined as the ratio between maximum and minimum value. Compares to figure 2.5.

7

Results

In this section, the obtained results are presented along with the corresponding statistical analysis, while the meanings and implications are discussed in chapter 8.

7.1 RVEF values

As described in sections 6.2 and 6.3, data from 13 patients were analysed. For each patient, 12 reconstructions were made and two ROIs drawn, yielding a total of 312 values for RVEF, which are presented in table 7.1. An initial overview of the values are presented in figure 7.1a, where the mean values obtained by PET are plotted against the values found by MRI.

In general, the estimates found by PET are significantly lower than those found by MRI, as illustrated in figure 7.1b. Otherwise, the variation in the obtained values appear to be similar for PET and MRI. The underestimation by PET is discussed in section 8.3.

Two patients, 1 and 18, have relatively high values of RVEF measured by MRI, 75.3% and 76.1%, respectively. This is outside the reported normal range, as described in section 4.5. Across the different bin sizes and reconstruction algorithms, these two patients have relatively low estimates of RVEF by PET.

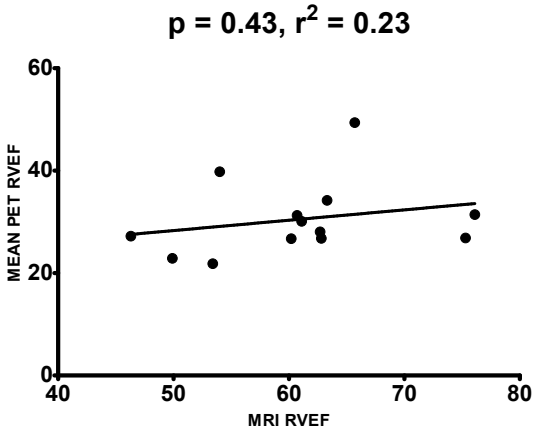

(a) Mean value estimated by PET for each patient across various bin sizes and reconstruction algorithms, plotted against the corresponding values found by MRI.

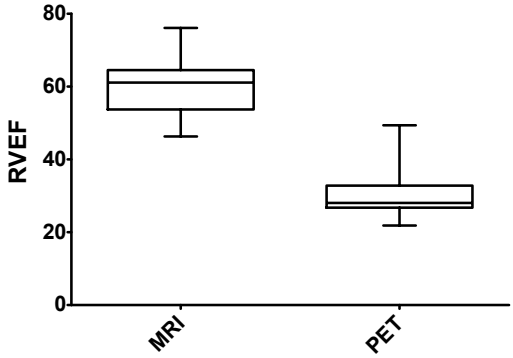

(b) Mean values estimated by PET and MRI, illustrating the general underestimation seen in PET. The whiskers show maximum and minimum values.

Figure 7.1 – Initial overview of the RVEF values obtained and their comparison to those found by MRI. Based on mean values across bin sizes and reconstruction algorithms.

	Sex	Age	Weight [kg]	FBP			OSEM2D			OSEM3D			TRUE X			MRI
				8	12	16	8	12	16	8	12	16	8	12	16	
1	F	36	50	26.7	27.9	29.2	22.0	22.3	22.0	25.0	25.0	28.6	25.2	25.6	28.7	75.3
				29.0	29.5	32.6	24.1	23.6	24.9	27.2	26.8	30.9	28.0	27.6	31.6	
4	F	36	75	28.6	28.3	39.9	25.5	25.3	32.3	26.2	26.7	36.3	26.2	26.6	36.3	60.7
				30.9	32.5	40.8	28.4	28.7	35.2	28.8	30.8	37.9	28.9	31.0	38.1	
5	F	41	59	24.6	27.6	28.2	21.9	24.0	23.2	24.3	25.6	27.1	24.3	25.5	27.2	62.8
				28.9	30.5	31.8	25.3	26.4	26.0	26.9	28.0	29.2	27.3	28.7	30.0	
6	F	76	73	44.6	47.2	47.0	35.7	34.8	34.0	38.9	39.9	40.3	39.3	40.6	41.4	54.0
				40.7	42.7	45.5	35.5	33.9	34.8	38.0	38.5	41.4	38.3	38.9	42.5	
9	F	71	65	45.9	52.9	52.3	40.7	45.7	44.0	41.7	50.7	46.5	41.9	51.2	49.2	65.7
				50.9	57.6	57.0	45.0	46.9	47.4	47.4	55.1	53.1	47.9	55.8	53.7	
11	M	39	102	22.1	25.3	25.1	18.2	18.9	17.8	21.0	23.1	23.1	21.1	23.30	23.1	49.9
				23.7	27.2	27.8	20.0	20.6	20.5	22.5	24.6	25.6	22.8	25.2	26.2	
12	F	43	78	28.1	27.9	33.0	24.9	23.5	27.2	26.8	26.0	31.9	27.1	26.1	33.1	60.2
				24.9	23.3	28.2	23.7	21.9	25.0	24.9	23.3	30.4	25.2	23.3	31.3	
13	F	43	72	26.5	37.7	33.4	22.5	30.5	25.9	25.1	35.6	32.9	25.2	35.8	33.1	61.1
				27.3	33.0	30.5	24.8	30.7	27.3	26.4	33.9	31.8	26.4	33.7	32.3	
14	M	43	95	28.7	27.2	32.2	26.2	22.4	28.3	27.0	24.2	30.8	27.4	24.8	31.5	46.3
				27.7	25.6	30.5	26.2	22.1	27.8	26.7	23.8	29.6	27.1	24.5	30.3	
18	F	63	50	26.2	29.4	33.8	23.6	25.9	29.5	25.4	27.8	32.7	25.3	28.2	32.4	76.1
				33.4	36.6	38.8	29.6	32.4	33.4	31.8	35.1	37.0	32.6	35.7	37.0	
19	M	61	70	20.8	21.2	21.1	19.8	19.5	19.9	21.12	21.8	21.8	21.1	21.8	21.9	53.4
				22.4	22.7	22.9	21.4	20.9	21.7	22.8	23.3	23.7	22.9	23.4	23.9	
20	F	63	71	37.5	31.0	32.4	34.3	24.9	25.9	35.6	29.6	30.4	36.1	30.7	31.9	62.7
				30.0	23.0	23.9	29.1	19.7	19.2	29.0	21.8	22.7	28.9	22.4	23.1	
21	F	55	58	29.1	29.3	34.4	25.0	23.9	25.8	28.8	30.0	35.6	28.6	29.5	35.7	63.3
				38.7	41.9	42.7	31.3	32.5	30.6	38.8	42.2	41.5	39.6	42.2	42.4	

Table 7.1 – Computed values for RVEF in percent for different reconstruction algorithms and number of bins.

7.2 ANOVA

Table 7.1 presents the analysis of variance, performed with R [28] and according to the model described in section 4.3.4. The analysis shows that all considered factors are significant, both bin size, reconstruction algorithm and their interaction. Patient variability is expected, and incorporated into the model, but not estimated.

Figure 7.2 show the mean RVEF found by PET for each of the factors considered. There is a highly significant difference between FBP and OSEM2D, while there are no significant difference between OSEM3D and TRUEX, but they are significantly different from OSEM2D (not shown).

Generally, the estimate for RVEF by PET increases with the number of bins used, with a significant difference of 3.1 EF units between 8 and 16 bins, which is consistent with the literature [11]. A students t-test between these two bin sizes yield a p-value of 0.0011.

	DF	Sum Sq	Mean Sq	F value	Pr(>F)
Bin size	2	512.98	256.49	5.06	0.0146
Error	24	1215.45	50.64		
Reconstruction method	3	1092.24	364.08	47.48	< 0.001
Error	36	276.06	7.67		
Interaction	6	80.43	13.40	24.44	< 0.001
Error	72	39.49	0.55		
Error between patients	12	15565.81	1297.15		
Error within patients (ROI)	156	1509.54	9.68		

Table 7.2 – ANOVA analysis of the obtained RVEF values, evaluating the influence of the factors bin size and reconstruction method. Patients are included as a random factor.

7.3 Correlations

Using estimates from all 13 patients as listed in table 7.1, no correlation between the values obtained using PET and those found by MRI are observed. This is illustrated for the mean values in figure 7.1a and listed in table 7.3 as probabilities and correlation coefficients.

As noted earlier, two patients have relatively high RVEF values found by MRI. By designating these two and a third patient as *outliers*, a modified dataset is created. Patients 1, 4 and 10 are excluded, bringing the modified set of estimates down to 10 patients. Here, indications of a correlation can be seen using 8 bins and OSEM3D, $p = 0.0589$ and $r^2 = 0.38$. Full correlation analysis is listed in table 7.3, and the two combinations with the best correlation is plotted in figure 7.3.

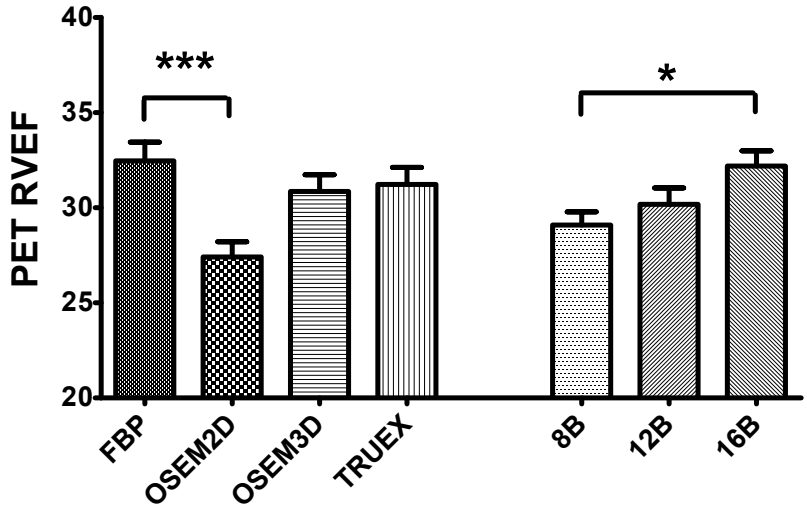

Figure 7.2 – Statistical analysis of the mean values found using different reconstruction methods and bin sizes. Patient variability has not been taken into account.

	Full data-set		Outliers removed	
	p	r^2	p	r^2
8B FBP	0.5443	0.034	0.0684	0.36
12B FBP	0.4676	0.049	0.0820	0.33
16B FBP	0.4519	0.052	0.1026	0.30
8B OSEM2D	0.6068	0.025	0.0865	0.32
12B OSEM2D	0.3599	0.077	0.0665	0.36
16B OSEM2D	0.4699	0.048	0.1663	0.22
8B OSEM3D	0.5080	0.041	0.0589	0.38
12B OSEM3D	0.4029	0.064	0.0621	0.37
16B OSEM3D	0.3653	0.075	0.0862	0.32
8B TRUEX	0.4970	0.043	0.0629	0.37
12B TRUEX	0.3950	0.066	0.0661	0.36
16B TRUEX	0.3992	0.066	0.0832	0.33

Table 7.3 – Probability values and correlation coefficients for linear correlation between RVEF values estimated by PET and MRI. Full result is all measurements, and the modified result is with the removal of outliers.

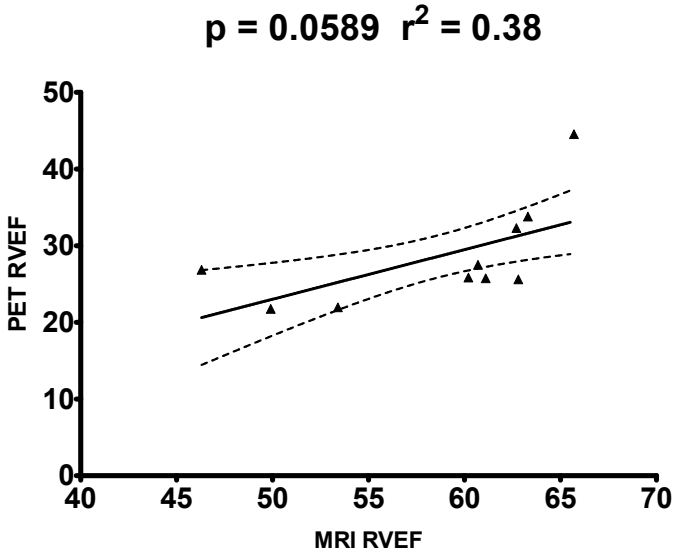

(a) 8 bins, OSEM3D

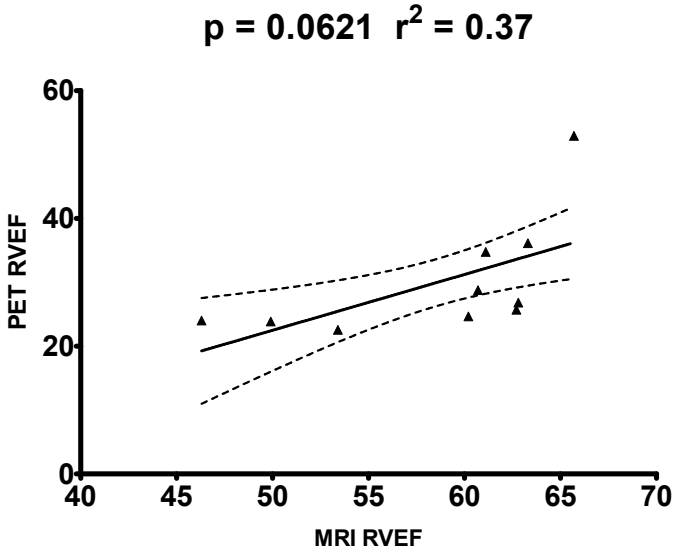

(b) 12 bins, OSEM3D

Figure 7.3 – Correlation between mean RVEF values found by MRI and PET for the two combinations of bin size and reconstruction method that showed best correlation. Outliers are removed, giving n=10 patients.

8

Discussion

Given a novel understanding of PET imaging and first-pass RNV, the concept of applying the first-pass technique to PET seems obvious and straightforward. Some technical challenges were clear from the beginning, and more arose during the project. This section elaborates on the experiences and results gained from the project up until now.

8.1 Approach to temporal sampling

From the beginning of the projects, the challenge of achieving temporal resolution below 500 ms was obvious, as this had been the primary reason for pausing the study at an earlier stage. The initial approach was to process the list-mode file outside the scanner environment, using custom made software. This approach is preferable over the ECG-gating approach described in section 6.1.2, as it does not make any assumptions on cardiac cycle regularity. The count rate appear to be high enough to make meaningful images at such short periods, as PET has a considerably higher sensitivity compared to gamma cameras due to the coincidence collimation.

Some achievements were made along this approach, as custom software for histogramming certain versions of the list-mode file was actually obtained. However, each step further presented several new challenges. Siemens has put considerable efforts into sealing the internal mechanisms of image reconstruction, hence it does not appear feasible to continue exploring this approach without a collaboration with Siemens. Furthermore, this approach requires substantial computer programming experience. The current clinical workstation software can presumably be modified quite easily to handle frame durations less than 1 seconds; I suspect it to be merely an interface-issue.

8.2 ECG-gating approach

As it became clear that the list-mode approach was beyond the scope of this project, the ECG-gating solution was implemented. This is based on the assumption that the ratio of tracer is constant for each cardiac cycle under the bolus passage, as described in section 6.1.2. The assumption is also applied in traditional RNV, and any uncertainties introduced from this assumption should be inferior compared to other uncertainties.

The duration of the reconstruction period is another variable. In this study, a period of 4-6 seconds was chosen from the initial time-activity curve, corresponding to the primary part of the bolus passage. This was done on a rather subjective basis, and could be formalised further. Also, several reconstructions with varying duration and onset could be made in order to investigate the impact on the absolute RVEF estimate and correlation to MRI.

8.3 Underestimation of RVEF

While current MRI protocols have a tendency to overestimate the absolute value of RVEF, the method presented here clearly underestimates the value of RVEF in its current form. The absolute values for RVEF is of less importance, given that a clear correlation with other modalities can be established, although an accurate absolute value would be preferable. The correlation is discussed in section 8.4.

Several effects can be considered responsible for the underestimation. The analysis of variance, presented in section 7.2, states that all considered factors are significant. However, the importance of an accurate ROI appears predominant, especially for separating the atrium and ventricle. By including parts of the atrium in the ROI, this volume will contribute equally to the EDV and ESV, making the ratio between them smaller. As the significance of a correct ROI was realised rather late in the course of the project, none of the many initiatives towards ensuring a more precise drawing was investigated. Initiatives towards this are discussed further in section 8.7.

8.4 Correlation with MRI

One of the primary goals of this project was to establish a clear correlation between values for RVEF obtained by FDG-PET and those found using cMRI. While there are indications that such a correlation can be established, the results of this project does not form a basis for this conclusion.

Two of the thirteen patients were found by cMRI to have an RVEF of 75.3 and 76.1 %, respectively. These values are considered outside of the normal range, even by those

normally found by MRI, as described in section 4.5. In parallel, these two patient are found by the PET method to have relatively low values of RVEF. By removing these two patients and a third outlier, the dataset is reduced to 10 patients, and correlation between the two modalities are evident. Although it would be a far-fetched to draw conclusions based on this, it induces a hope that a larger number of patients and improvements of the methods will show a definite correlation.

In this perspective, it is a shame that although 23 patients were involved in this study, only 13 had both scans. This is still a fairly high number of patients for such a comprehensive study, yet in the light of the current results, the feeling of a missed opportunity is still present.

8.5 Bin size

Another goal was to investigate the effect of various bin sizes. More bins mean higher temporal resolution, but less counts in each bins, which should equal more noisy images. In a traditional first-pass RNV, 16 to 32 bins are used, whereas most gated cardiac PET examinations use 8 or 16 bins according to Christensen et al. [11], who also states that EF is generally slightly under-estimated when using 8 bins compared to 16 for RNV examinations.

The analysis of variance in table 7.2 reveals that the bin size is a significant factor. However, no conclusions have been made as to which number is the best. Based on the individual example seen in figure 6.5, it is clear that the use of 16 bins give a more adequate impression of the volume change over time. The plateau seen during diastasis is not visible in the 8 bin curves, as opposed to in the 16 bins curves. When the objective is to estimate the EF, however, the bin size does not seem to be of high importance. The count rate appears to mere more than sufficient, hence there are no reason other than longer reconstruction times to avoid more bins.

8.6 Reconstruction algorithms

As described in section 6.2, there are fundamental differences in the way analytical and iterative reconstruction algorithms work. Figure 7.2 illustrate that there is a significant difference between the mean of the values found by FBP and OSEM2D, with OSEM3D and TRUEX placing themselves in-between. Iterative algorithms are generally preferred in the daily clinical routine, due to the superior image quality. However, the visual image quality is not important for estimating RVEF.

The quantitative performance was studied by [47], who found comparable quantitative results and visually better images using OSEM over FBP. Theoretically, iterative reconstruction algorithms can introduce quantitative errors, due to their non-linear nature. Com-

pared to several other PET examinations, first-pass studies have relatively high activities in a small volumes, which, along with short time frames represent extreme conditions for an iterative algorithm. However, there are no indications of severe, quantitative errors using the iterative algorithms in the present study. The difference for OSEM2D is presumably due to the two-dimensional nature, which alters the geometric properties of data recording.

Another influence on the quantitative values are the re-orientation. Transformation of images into short-axis view is standard practice, and also gives a better separation of the chambers, which should yield a more precise ROI. However, the re-orientation procedure can induce quantitative inaccuracies, as investigated by [33], due to the interpolation done. The amount of error induced should be investigated further, but it can not explain the underestimation of RVEF in the present study.

8.7 Perspectives

Several relevant improvements have already been indicated. Most imminent is the need for a more reliable methodology for constructing an ROI, especially for separating the right ventricle from the atrium. Until now, the designation of the atrioventricular septum has been made in short-axis view, but this does not appear to be the optimal way. It should be investigated whether the ventricle and atrium can be distinguished in horizontal long axis view.

The reconstruction made for ROI drawing could also be done with ECG-gating, enabling drawing of an ROI for each phase of the cardiac cycle. If a clear identification of the atrioventricular septum can be made, the effect of constructing phase-specific ROIs can be estimated. Retrospectively, a diagnostic CT-scan could also potentially be used for segmenting the right ventricle and form the basis of an ROI. This would however expose the patient to an significant amount of ionizing radiation.

Although the ECG-gating approach seems feasible, the list-mode approach would be interesting to follow through. Potentially, the possibility of constructing sub-second frames could be implemented in a future scanner workstation upgrade, if the relevant people at Siemens could be notified about this need. The choice of time window could also be investigated further. The list-mode data can be reconstructed in almost any way desired, hence a series of period placements and durations could be made, followed by an analysis of the RVEF values they yield.

Over the summer, the possibilities of constructing a better ROI will be examined. As the time-activity and volume curves appear to be in consistency with the literature, the belief is that further improvements will produce more physiological realistic estimates of RVEF and show a clear correlation with the values obtained by MRI.

9

Conclusion

In the period of October 2008 to June 2009, a remarkable PET dataset was created at Rigshospitalet. The purpose was to prove that RVEF could be estimated during a routinely performed FDG-PET scan, thereby relieving relevant patients of an extra examination. This has the potential to increase cost-effectiveness, reduce the dose of ionising radiation administered to the patient and primarily make things easier for the individuals finding themselves in an already difficult situation. A total of 13 patients, mean age 51.4 $\pm$ 12 years, underwent list-mode recording during the first-pass of the FDG bolus through the heart, where it is confined to the right side. Furthermore, the patients were scanned with MRI for validation.

Estimation of RVEF using first-pass PET introduced several technical challenges, which are addressed in this thesis. In order to capture the cardiac contraction, the Nyquist theorem dictates a temporal sampling of at least twice the heart-rate. The clinical workstations at Rigshospitalet are not capable of making direct frame rates below 1 second, which are required to be in the order of 100-200 ms. This was solved by making 4-6 seconds of ECG-gated reconstructions during the FDG bolus passage, with each cardiac cycle divided into a number of bins. Reconstructions were made with different number of bins and reconstruction algorithms, in order to evaluate their influence on the RVEF estimate.

Another challenge turned out to be constructing a precise ROI. All images were re-oriented into short-axis view, which provided for easier separation between the left and right side. It is still challenging to divide the atrium and ventricle in this view. Including parts of the atrium in the ROI will lead to a lower RVEF than expected, which is also observed in this thesis. A mean RVEF value of 33 % across patients was found using PET and 16 bins, compared to 61 % for MRI. Using 8 bins gave average estimates of about 4 EFunits lower, which corresponds to previously published results. Using FBP for reconstruction resulted in a significantly higher estimate of RVEF compared to using OSEM2D.

The primary objective was to document a correlation between the values obtained by first-pass FDG-PET and MRI. No immediate correlation was found on the full dataset. By removing 3 outliers from the dataset, a significant correlation was proved between

RVEF value obtained by MRI and FDG-PET using 8 bins and OSEM3D ($n = 10, p = 0.0583, r^2 = 0.38$).

In order to improve this technique, a routine for better and more consistent ROI-drawing must be enabled. The use of separate ROIs for end-systole and end-diastole should also be examined, due to the contractile movement of right ventricle. It would also be interesting to examine which phases of the first-pass passage should be included in the reconstruction. A more accurate ROI is expected to result in RVEF estimates comparable to those found by existing techniques found in the clinic today. The work of achieving this will continue over the next months, and if successful, a larger study should be performed to verify the accuracy, before a clinical routine is established.

Bibliography

[1] *Cardiac Computed Tomography*, pages 72–91. Wiley-Blackwell, 2010. ISBN 9781444323894. doi: 10.1002/9781444323894.ch3. URL http://dx.doi.org/10.1002/9781444323894.ch3.

[2] *Cardiovascular Magnetic Resonance: Basic Principles, Methods, and Techniques*, pages 30–71. Wiley-Blackwell, 2010. ISBN 9781444323894. doi: 10.1002/9781444323894.ch2. URL http://dx.doi.org/10.1002/9781444323894.ch2.

[3] Thomas Beyer, DW Townsend, and Tony Brun. A combined PET/CT scanner for clinical oncology. *Journal of Nuclear Medicine*, 41(8):1369–1379, 2000. URL http://faculty.washington.edu/kinahan/publications/Beyer_JNM2000.pdf.

[4] G B Bleeker, P Steendijk, E R Holman, C-M Yu, O a Breithardt, T a M Kaandorp, M J Schalij, E E van der Wall, P Nihoyannopoulos, and J J Bax. Assessing right ventricular function: the role of echocardiography and complementary technologies. *Heart (British Cardiac Society)*, 92 Suppl 1(fig 2):i19–26, April 2006. ISSN 1468-201X. doi: 10.1136/hrt.2005.082503. URL http://www.pubmedcentral.nih.gov/articlerender.fcgi?artid=1860734&tool=pmcentrez&rendertype=abstract.

[5] J. Bogaert. *Clinical Cardiac MRI*. Medical Radiology. Springer, 2012. ISBN 9783642230356. URL http://books.google.dk/books?id=Cuz4ayP8rZkC.

[6] R.O. Bonow, D.L. Mann, D.P. Zipes, and P. Libby. *Braunwald's Heart Disease E-Book: A Textbook of Cardiovascular Medicine, 2-Volume Set*. Elsevier Health Sciences, 2011. ISBN 9781437727708. URL http://books.google.dk/books?id=b5wADkB9oDoC.

[7] Darrell D Burckhardt. Cardiac Positron Emission Tomography: Overview of Myocardial Perfusion, Myocardial Blood Flow and Coronary Flow Reserve Imaging. 2009.

[8] Jerrold T. Bushberg, J. Anthony Seibert, Edwin M. Leidholt, and John M. Boone. *The Essential Physics of Medical Imaging*. Lippincott Williams & Wilkins, second edition edition, 2002.

[9] M Cerqueira. Standardized myocardial segmentation and nomenclature for tomographic imaging of the heart: A statement for healthcare professionals from the Cardiac Imaging Committee of the Council on Clinical Cardiology of the American Heart Association. *Journal of Nuclear Cardiology*, 9(2):240–245, March 2002. ISSN 10713581. doi: 10.1067/mnc.2002.123122. URL http://linkinghub.elsevier.com/retrieve/pii/S1071358102490496.

[10] EQ Chen, WJ MacIntyre, and FM Fouad. Measurement of cardiac output with first-pass determination during rubidium-82 PET myocardial perfusion imaging. *European Journal of Nuclear Medicine*, 23(8):993–996, 1996. URL http://www.springerlink.com/index/t4021701658j1n72.pdf.

[11] Charlotte Birk Christensen, Annika Loft, and Birger Hesse, editors. *Klinisk Nuklearmedicin*, volume 1. Dansk Selskab for Klinisk Fysiologi og Nuklearmedicin, 2 edition, 2011.

[12] Rune Christensen. Calculation of right ventricular function in rats on basis of first-pass data acquired with pet and spect - a bachelor project, 2007.

[13] S J Cullom, J a Case, and T M Bateman. Electrocardiographically gated myocardial perfusion SPECT: technical principles and quality control considerations. *Journal of nuclear cardiology : official publication of the American Society of Nuclear Cardiology*, 5(4):418–25, 1998. ISSN 1071-3581. URL http://www.ncbi.nlm.nih.gov/pubmed/9715987.

[14] F Daghighian, P Shenderov, K.S. Pentlow, M.C. Graham, and B. Eshaghian. Evaluation of cerium doped lutetium oxyorthosilicate (LSO) scintillation crystals for PET. *IEEE Transactions on Nuclear Science*, 40(4):1045–1047, 1993. URL http://ieeexplore.ieee.org/xpls/abs_all.jsp?arnumber=256710.

[15] Robertson Davenport and Ann Arbor. The Derivation of the Gamma-Variate Relationship for Tracer Dilution Curves. *Journal of nuclear medicine : official publication, Society of Nuclear Medicine*, 24(10):945–948, 1983.

[16] P de Groote, a Millaire, C Foucher-Hossein, O Nugue, X Marchandise, G Ducloux, and J M Lablanche. Right ventricular ejection fraction is an independent predictor of survival in patients with moderate heart failure. *Journal of the American College of Cardiology*, 32(4):948–54, October 1998. ISSN 0735-1097. URL http://www.ncbi.nlm.nih.gov/pubmed/9768716.

[17] M.F. Di Carli and M.J. Lipton. *Cardiac Pet and Pet/CT Imaging*. Springer, 2007. ISBN 9780387352756. URL http://books.google.dk/books?id=JCQ8V3V1RtoC.

[18] T G Di Salvo, M Mathier, M J Semigran, and G W Dec. Preserved right ventricular ejection fraction predicts exercise capacity and survival in advanced heart failure. *Journal of the American College of Cardiology*, 25(5):1143–53, April 1995. ISSN 0735-1097. URL http://www.ncbi.nlm.nih.gov/pubmed/7897128.

[19] Gregory Z Ferl, Xiaoli Zhang, Hsiao-Ming Wu, Michael C Kreissl, and Sung-Cheng Huang. Estimation of the 18F-FDG input function in mice by use of dynamic small-animal PET and minimal blood sample data. *Journal of nuclear medicine : official publication, Society of Nuclear Medicine*, 48(12):2037–45, December 2007. ISSN 0161-5505. doi: 10.2967/jnumed.107.041061. URL http://www.ncbi.nlm.nih.gov/pubmed/18006615.

[20] John D. Friedman, Daniel S. Berman, Salvador Borges-Neto, Sean W. Hayes, Lynne L. Johnson, Kenneth J. Nichols, Robert a. Pagnanelli, and Steven C. Port. ASNC Announcement - First-pass radionuclide angiography. *Journal of Nuclear Cardiology*,

16(2):330–330, February 2009. ISSN 1071-3581. doi: 10.1007/s12350-009-9061-5. URL http://www.springerlink.com/index/10.1007/s12350-009-9061-5.

[21] J. Gomme. *Isotopteknik: Radioaktive isotoper og ioniserende stråling i biologi og medicin*. Gad, 1997. ISBN 9788712030485. URL http://books.google.dk/books?id=75weQwAACAAJ.

[22] Henrik Gutte. *Neuroendocrine activation and diagnostics in pulmonary embolism: Translational studies*. PhD thesis, University of Copenhagen, 2010.

[23] Y-x He and Q-y Guo. Clinical applications and advances of positron emission tomography with fluorine-18-fluorodeoxyglucose (18F-FDG) in the diagnosis of liver neoplasms. *Postgraduate medical journal*, 84(991):246–51, May 2008. ISSN 1469-0756. doi: 10.1136/pgmj.2007.066589. URL http://www.ncbi.nlm.nih.gov/pubmed/18508981.

[24] B Hesse, K Tägil, a Cuocolo, C Anagnostopoulos, M Bardiés, J Bax, F Bengel, E Busemann Sokole, G Davies, M Dondi, L Edenbrandt, P Franken, a Kjaer, J Knuuti, M Lassmann, M Ljungberg, C Marcassa, P Y Marie, F McKiddie, M O'Connor, E Prvulovich, R Underwood, and B van Eck-Smit. EANM/ESC procedural guidelines for myocardial perfusion imaging in nuclear cardiology. *European journal of nuclear medicine and molecular imaging*, 32(7):855–97, July 2005. ISSN 1619-7070. doi: 10.1007/s00259-005-1779-y. URL http://www.ncbi.nlm.nih.gov/pubmed/15909197.

[25] B Hesse, T B Lindhardt, W Acampa, C Anagnostopoulos, J Ballinger, J J Bax, L Edenbrandt, a Flotats, G Germano, T Gmeiner Stopar, P Franken, a Kelion, a Kjaer, D Le Guludec, M Ljungberg, a F Maenhout, C Marcassa, J Marving, F McKiddie, W M Schaefer, L Stegger, and R Underwood. *EANM/ESC guidelines for radionuclide imaging of cardiac function.*, volume 35. April 2008. ISBN 0025900706. doi: 10.1007/s00259-007-0694-9. URL http://www.ncbi.nlm.nih.gov/pubmed/18224320.

[26] G Hevesy. The Absorbtion and Translocation of Lead by Plants. A Contribution to the Application of the Method of Radioactive Indicators in the Investigation of the Change of Substance in Plants. *Biochemical Journal*, 1923. URL http://www.ncbi.nlm.nih.gov/pmc/articles/PMC1263906/.

[27] S Y Ho and P Nihoyannopoulos. Anatomy, echocardiography, and normal right ventricular dimensions. *Heart (British Cardiac Society)*, 92 Suppl 1(C):i2–13, April 2006. ISSN 1468-201X. doi: 10.1136/hrt.2005.077875. URL http://www.pubmedcentral.nih.gov/articlerender.fcgi?artid=1860731&tool=pmcentrez&rendertype=abstract.

[28] Kurt Hornik. The R FAQ, 2011. URL http://CRAN.R-project.org/doc/FAQ/R-FAQ.html. ISBN 3-900051-08-9.

[29] GN Hounsfield. Computerized transverse axial scanning (tomography): Part 1. Description of system. *British Journal of Radiology*, 46(552):1016–1022, 1973. URL http://bjr.birjournals.org/content/46/552/1016.short.

[30] H.M. Hudson and R.S. Larkin. Accelerated Image Reconstruction using Ordered Subsets of Projection Data. *Medical Imaging, IEEE Transactions on*, 13(4):601–609, 1994. URL http://ieeexplore.ieee.org/xpls/abs_all.jsp?arnumber=363108.

[31] PE Kinahan, DW Townsend, and T Beyer. Attenuation correction for a combined 3D PET/CT scanner. *Medical physics*, 25(10):2046–2053, 1998. URL http://link.aip.org/link/?MPHYA6/25/2046/1.

[32] Michael C Kreissl, Hsiao-Ming Wu, David B Stout, Waldemar Ladno, Thomas H Schindler, Xiaoli Zhang, John O Prior, Mayumi L Prins, Arion F Chatziioannou, Sung-Cheng Huang, and Heinrich R Schelbert. Noninvasive measurement of cardiovascular function in mice with high-temporal-resolution small-animal PET. *Journal of nuclear medicine : official publication, Society of Nuclear Medicine*, 47(6):974–80, June 2006. ISSN 0161-5505. URL http://www.ncbi.nlm.nih.gov/pubmed/16741307.

[33] W G Kuhle, G Porenta, S C Huang, M E Phelps, and H R Schelbert. Issues in the quantitation of reoriented cardiac PET images. *Journal of nuclear medicine : official publication, Society of Nuclear Medicine*, 33(6):1235–42, June 1992. ISSN 0161-5505. URL http://www.ncbi.nlm.nih.gov/pubmed/1597745.

[34] W. Mohnike, G. Hör, and H.R. Schelbert. *Oncologic and Cardiologic Pet/CT-Diagnosis: An Interdisciplinary Atlas and Manual*. Springer, 2008. ISBN 9783540740902. URL http://books.google.dk/books?id=kdybOMk_MVcC.

[35] D.C. Montgomery. *Design and Analysis of Experiments*. John Wiley & Sons, Limited, 7 edition, 2009. ISBN 9781118097939. URL http://books.google.dk/books?id=KSRZpwAACAAJ.

[36] N a Mullani and K L Gould. First-pass measurements of regional blood flow with external detectors. *Journal of nuclear medicine : official publication, Society of Nuclear Medicine*, 24(7):577–81, July 1983. ISSN 0161-5505. URL http://www.ncbi.nlm.nih.gov/pubmed/6602868.

[37] Brookhaven National Laboratory National Nuclear Data Center. Nudat (nuclear structure and decay data), 2008.

[38] P Oldershaw. Assessment of right ventricular function and its role in clinical practice. *British heart journal*, 68(1):12–5, July 1992. ISSN 0007-0769. URL http://www.pubmedcentral.nih.gov/articlerender.fcgi?artid=1024962&tool=pmcentrez&rendertype=abstract.

[39] E K Pauwels, M J Ribeiro, J H Stoot, V R McCready, M Bourguignon, and B Mazière. FDG accumulation and tumor biology. *Nuclear medicine and biology*, 25(4):317–22, May 1998. ISSN 0969-8051. URL http://www.ncbi.nlm.nih.gov/pubmed/9639291.

[40] M. E. Pfisterer, A. Battler, and B. L. Zaret. Range of normal values for left and right ventricular ejection fraction at rest and during exercise assessed by radionuclide angiocardiography. *European Heart Journal*, 6(8):647–655, 1985. URL http://eurheartj.oxfordjournals.org/content/6/8/647.abstract.

[41] M.E. Phelps, E.J. Hoffman, and N.A. Mullani. Application of annihilation coincidence detection to transaxial reconstruction tomography. *Journal of Nuclear Medicine*, 16 (3):210, 1975. URL http://ukpmc.ac.uk/abstract/MED/1113170.

[42] Michael E. Phelps. *PET: Physics, Instrumentation, and Scanners*. Springer, 2006.

[43] E.B. Podgoršak. *Radiation Physics for Medical Physicists*. Biological and Medical Physics, Biomedical Engineering. Springer, 2006. ISBN 9783540250418. URL http://books.google.dk/books?id=lkWRKVmTueUC.

[44] M B Rominger, G F Bachmann, W Pabst, and W S Rau. Right ventricular volumes and ejection fraction with fast cine MR imaging in breath-hold technique: applicability, normal values from 52 volunteers, and evaluation of 325 adult cardiac patients. *Journal of magnetic resonance imaging : JMRI*, 10(6):908–18, December 1999. ISSN 1053-1807. URL http://www.ncbi.nlm.nih.gov/pubmed/10581503.

[45] CE Shannon. Communication in the presence of noise. *Proceedings of the IRE*, 3(2), 1949. URL http://ieeexplore.ieee.org/xpls/abs_all.jsp?arnumber=1697831.

[46] *Biograph™ TruePoint PET ▪ CT*. Siemens Medical Solutions, 2007.

[47] Hanne M Sø ndergaard, Mette Marie Madsen, Karin Boisen, Morten Bø ttcher, Ole Schmitz, Torsten T Nielsen, Hans Erik Bø tker, and Søren B Hansen. Evaluation of iterative reconstruction (OSEM) versus filtered back-projection for the assessment of myocardial glucose uptake and myocardial perfusion using dynamic PET. *European journal of nuclear medicine and molecular imaging*, 34(3):320–9, March 2007. ISSN 1619-7070. doi: 10.1007/s00259-006-0198-z. URL http://www.ncbi.nlm.nih.gov/pubmed/17033850.

[48] J. Sobotta, R. Putz, R. Pabst, and S. Bedoui. *Sobotta Atlas of Human Anatomy*, volume One Volume Edition of *Atlas of Human Anatomy (Sobotta) Series*. Elsevier Urban & Fisher, 14th edition, 2006. ISBN 978-0-7020-3483-1.

[49] S. Standring and H. Gray. *Gray's Anatomy: The Anatomical Basis of Clinical Practice*. Gray's Anatomy: The Anatomical Basis of Clinical Practice. Churchill Livingstone/Elsevier, 2008. ISBN 9780443066849. URL http://books.google.dk/books?id=kvhkPQAACAAJ.

[50] The Georgia State and Georgia Tech Center for Advanced Brain Imaging. [image] - sampling theory. http://www.cabiatl.com/CABI/resources/part/.

[51] USA. Texas Heart Institute. [image] - heart anatomy. http://www.texasheartinstitute.org/HIC/Anatomy/anatomy2.cfm.

[52] Department of Medical Physics University College London and Bioengineering. Interfile archive. http://www.medphys.ucl.ac.uk/interfile/.

[53] E.P. Widmaier, H. Raff, and K.T. Strang. *Vander's human physiology: the mechanisms of body function*. McGraw-Hill Higher Education, 2008. ISBN 9780073049625. URL http://books.google.dk/books?id=7GRqAAAAMAAJ.

[54] H.M. Wu, M.C. Kreissl, H.R. Schelbert, Waldemar Ladno, Mayumi Prins, K. Shoghi-Jadid, Arion Chatziioannou, M.E. Phelps, and S.C. Huang. First-pass angiography in mice using FDG-PET: a simple method of deriving the cardiovascular transit time without the need of region-of-interest drawing. *Nuclear Science, IEEE Transactions on*, 52(5):1311–1315, 2005. URL http://ieeexplore.ieee.org/xpls/abs_all.jsp?arnumber=1546412.

A

MATLAB code

A.1 Main script for each patient

```
% Script for processing individual patient data.
%
% This script is modified for each patient and provides the routine for
% estimating RVEF. Uses different sub-functions developed ...
    specific for
% this project.

% Copyright Andreas Clemmensen, 2012

clear all; close all;
set(0,'DefaultFigureWindowStyle','docked') ;
set(0,'defaultlinelinewidth',2)
set(0,'defaultpatchlinewidth',2)
set(0,'DefaultAxesFontSize',16)

% Pre-allocate
pt11_EF = zeros(12,1);

% Patient specific data
pt11_slices = [45,90,70]; % Slices to show on non-rotated data
pt11_slices_rot = [60,70,85]; % Slices to show on rotated data

% Defining ROI in short-axis planes
pt11_l_slice = 22;
pt11_u_slice = 55;

% Threshold for intensity in images
pt11_max = 18000;

% Load static 900 seconds image
pt11_img900 = dicom2mat('11/11_STATIC_900_FBP/');

```

```
% Compute rotation
[pt11_T,pt11_ang] = com_rot(pt11_img900,pt11_slices, pt11_max);
pt11_img900_rot = rot2sa(pt11_img900,pt11_T,pt11_slices_rot,pt11_max);

% Displays rotation angles
disp(['Patient 11 rotation angles:  ',num2str(pt11_ang)])

% Load masking data
pt11_ct = ctdicom2mat(2,'path-to-patient-data');
pt11_img300 = dicom2mat('11/11_STATIC_300_FBP/');

% Rotate images
pt11_ct_rot = rot2sa(pt11_ct,pt11_T);
pt11_img300_rot = rot2sa(pt11_img300,pt11_T);

% Draw ROI
pt11_voi = draw_mask(pt11_img300_rot,pt11_ct_rot,...
    pt11_l_slice,pt11_u_slice);

% Load dynamic bolus pass reconstruction
pt11_initial = dicom2mat('11/11_INITIAL_0_20_OSEM2D/');
% Produce images in background
view_initial(pt11_initial,pt11_ct,65);

% Create time-activity curve and gamma variate fit
pt11_tac = create_tac(pt11_initial,pt11_T,pt11_voi);
print('-depsc2','-f1','/Volumes/VERBATIM HD/FP_Results/pt11_tac.eps');

%% Processing each reconstruction
% FBP
[pt11_EF_8B_FBP,pt11_act_8B_FBP] = ...
    FP_wrapper('11/11_MAIN_9_6_8B_FBP/',...
    pt11_T, pt11_voi); pt11_EF(1) = pt11_EF_8B_FBP;
[pt11_EF_12B_FBP,pt11_act_12B_FBP] = ...
    FP_wrapper('11/11_MAIN_9_6_12B_FBP/',...
    pt11_T, pt11_voi); pt11_EF(2) = pt11_EF_12B_FBP;
[pt11_EF_16B_FBP,pt11_act_16B_FBP] = ...
    FP_wrapper('11/11_MAIN_9_6_16B_FBP/',...
    pt11_T, pt11_voi); pt11_EF(3) = pt11_EF_16B_FBP;

% OSEM2D
[pt11_EF_8B_OSEM2D,pt11_act_8B_OSEM2D] = ...
    FP_wrapper('11/11_MAIN_9_6_8B_OSEM2D/', pt11_T, pt11_voi);
pt11_EF(4) = pt11_EF_8B_OSEM2D;
[pt11_EF_12B_OSEM2D,pt11_act_12B_OSEM2D] = ...
    FP_wrapper('11/11_MAIN_9_6_12B_OSEM2D/', pt11_T, pt11_voi);
pt11_EF(5) = pt11_EF_12B_OSEM2D;
[pt11_EF_16B_OSEM2D,pt11_act_16B_OSEM2D] = ...
    FP_wrapper('11/11_MAIN_9_6_16B_OSEM2D/', pt11_T, pt11_voi);
pt11_EF(6) = pt11_EF_16B_OSEM2D;

% OSEM3D
[pt11_EF_8B_OSEM3D,pt11_act_8B_OSEM3D] = ...
    FP_wrapper('11/11_MAIN_9_6_8B_OSEM3D/', pt11_T, pt11_voi);
pt11_EF(7) = pt11_EF_8B_OSEM3D;
```

```
80 [pt11_EF_12B_OSEM3D,pt11_act_12B_OSEM3D] = ...
       FP_wrapper('11/11_MAIN_9_6_12B_OSEM3D/', pt11_T, pt11_voi);
81 pt11_EF(8) = pt11_EF_12B_OSEM3D;
82 [pt11_EF_16B_OSEM3D,pt11_act_16B_OSEM3D] = ...
       FP_wrapper('11/11_MAIN_9_6_16B_OSEM3D/', pt11_T, pt11_voi);
83 pt11_EF(9) = pt11_EF_16B_OSEM3D;
84
85 % TRUEX
86 [pt11_EF_8B_TRUEX,pt11_act_8B_TRUEX] = ...
       FP_wrapper('11/11_MAIN_9_6_8B_TRUEX/', pt11_T, pt11_voi);
87 pt11_EF(10) = pt11_EF_8B_TRUEX;
88 [pt11_EF_12B_TRUEX,pt11_act_12B_TRUEX] = ...
       FP_wrapper('11/11_MAIN_9_6_12B_TRUEX/', pt11_T, pt11_voi);
89 pt11_EF(11) = pt11_EF_12B_TRUEX;
90 [pt11_EF_16B_TRUEX,pt11_act_16B_TRUEX] = ...
       FP_wrapper('11/11_MAIN_9_6_16B_TRUEX/', pt11_T, pt11_voi);
91 pt11_EF(12) = pt11_EF_16B_TRUEX;
92
93 % Display result
94 disp('RVEF for patient 11:'); disp(pt11_EF')
95
96 %% Storing values to disk
97 disp('Saving...');
98 save('/Volumes/VERBATIM HD/FP_Results/pt11_v2.mat');
99 disp('done.');
```

A.2 Script for loading DICOM files - dicom2mat

```
1  function img = dicom2mat(varargin)
2  %IMG = DICOM2MAT Loading DICOM files into MATLAB structure.
3  % DICOM2MAT load all DICOM files in a series and gathers them in a ...
       3D or 4D
4  % MATLAB structure.
5  %
6  % If no input argument is given, the user will be asked to select a ...
       folder
7  % containing the DICOM files. Alternatively, the path to desired ...
       folder can
8  % be given as an input parameter.
9  %
10 % The script is written specifically for my Master thesis, hence makes
11 % certain assumptions, such that each 3D image consists of 111 ...
       transaxial
12 % slices.
13
14 % Copyright Andreas Clemmensen, 2012
15
16 % Define path to folder containing files
17 if nargin == 0
18     % Choose folder
19     dir_name = uigetdir('/Volumes/VERBATIM HD/FP_Main/', '');
20     dir_name = [dir_name,'/'];
```

```
21 elseif nargin == 1
22     dir_name = ['/Volumes/VERBATIM HD/FP_Main/',varargin{1}];
23 else
24     error('FIPATO:dicom2mat:InvalidParam','Only one input');
25 end
26
27 % Display directory
28 disp(['loading: ',dir_name]);
29
30 % Pre-allocate
31 listing = dir(dir_name);
32 n_frames = (size(listing,1)-2)/111;
33
34 % Counting and showing progress
35 i = 1; textprogressbar('loading DICOM files: ');
36
37 % Processing all files in the given directory
38 while ~...
       isempty(dir([dir_name,'*.PT.*(ADULT).*.',num2str(i),'.2012.*.IMA']))
39
40     name=dir([dir_name,'*.PT.*(ADULT).*.',num2str(i),'.2012.*.IMA']);
41     info=dicominfo([dir_name,name.name]);
42
43     % Extracting image and scaling correctly
44     tempimg = info.RescaleSlope*double(dicomread([dir_name,...
45         name.name]))-info.RescaleIntercept;
46
47     % Pre-allocating
48     if i == 1
49         imgsize = size(tempimg);
50         rawimg = zeros(imgsize(1),imgsize(2),111*n_frames);
51     end
52
53     % Storing image
54     rawimg(:,:,i) = tempimg;
55
56     % Show progress and increment count
57     textprogressbar(i*100/(111*n_frames)); i = i+1;
58 end
59
60 % Separating frames
61 rawframes = reshape(rawimg,imgsize(1),imgsize(2),111,n_frames);
62
63 % Flipping z-axis and removing air
64 if imgsize(1) == 336
65     img = flipdim(rawframes(104:231,104:231,:,:),3);
66 elseif imgsize(1) == 256
67     img = flipdim(rawframes(64:191,64:191,:,:),3);
68 else
69     img = flipdim(rawframes,3);
70 end
71
72 textprogressbar(' done');
```

A.3 Script for computing rotation - com_rot

```
function [T,ang] = com_rot(varargin)
%[T,ANG] = com_rot(VARARGIN) Computes rotation into
% short-axis view. Takes trans-axial images (IMG) for input, SLICES to
% use for drawing, and IMG_MAX as intensity trunkation.
%
% Output is a MATLAB transformation structure T, that contains the
% transformation matrix and other parameters. The computed angles ...
    are also
% output.

% Copyright Andreas Clemmensen, 2012

% Checking inputs
if nargin == 0
    error('FIPATO:com_rot:InvalidParam','No image input');
elseif nargin == 1
    img = varargin{1};
    if ndims(img) ~= 3
        error('FIPATO:com_rot:InvalidParam','Input image must have ...
            3 dimensions');
    end
    slices = [65,85,35];
elseif nargin == 2
    img = varargin{1};
    if ndims(img) ~= 3
        error('FIPATO:com_rot:InvalidParam','Input image must have ...
            3 dimensions');
    end
    slices = varargin{2};
    if numel(slices) ~= 3
        error('FIPATO:com_rot:InvalidParam','Number of slices must ...
            be 3');
    end
else
    error('FIPATO:com_rot:InvalidParam','Too many inputs');
end

% Pre-allocate
ang = zeros(size(slices));
close all;

% Create axis
l_111 = linspace(-111*2.0364/2,111*2.0364/2,111);
l_128 = linspace(-128*2.0364/2,128*2.0364/2,128);

% Defining initial range of shown values
base_CLim = [0 18000];
adj_CLim = base_CLim;

% Browsing slices in order to find the best ones.
while any(slices)
```

```
48      while any(slices(1))
49          % Opening figure and docking it
50          figure(1); set(1, 'WindowStyle', 'docked')
51          % Showing image with axes, title and labels
52          imagesc(l_111,l_128,squeeze(img(slices(1),:,:)));
53          xlabel('[mm]'); ylabel('[mm]'); colorbar;
54          title(['Coronal plane, slice no. ',num2str(slices(1))]);
55          % Setting range of values to pre-defined values
56          set(gca,'CLim',adj_CLim);
57          % Opening contrast adjustment window
58          c1 = imcontrast; set(c1, 'WindowStyle', 'docked')
59          % Offer possibility to change slice
60          slices(1) = input('Coronal slice OK? ');
61          % Saving adjusted intensity value
62          adj_CLim = get(gca,'CLim');
63      end
64      % Closing adjustment window and undocking figure
65      close(c1); set(1, 'WindowStyle', 'normal')
66      % Similar approach for other views
67      while any(slices(2))
68          figure(2); set(2, 'WindowStyle', 'docked')
69          imagesc(l_111,l_128,squeeze(img(:,slices(2),:)));
70          xlabel('[mm]'); ylabel('[mm]'); colorbar;
71          title(['Sagittal plane, slice no. ',num2str(slices(2))]);
72          set(gca,'CLim',adj_CLim);
73          c2 = imcontrast; set(c2, 'WindowStyle', 'docked')
74          slices(2) = input('Sigittal slice OK? ');
75          adj_CLim = get(gca,'CLim');
76
77      end
78      close(c2); set(2, 'WindowStyle', 'normal')
79      while any(slices(3))
80          figure(3); set(3, 'WindowStyle', 'docked')
81          imagesc(l_128,l_128,squeeze(img(:,:,slices(3))));
82          xlabel('[mm]'); ylabel('[mm]'); colorbar;
83          title(['Transversal plane, slice no. ',num2str(slices(3))]);
84          set(gca,'CLim',adj_CLim);
85
86          c3 = imcontrast; set(c3, 'WindowStyle', 'docked')
87          slices(3) = input('Transaxial slice OK? ');
88          adj_CLim = get(gca,'CLim');
89
90      end
91      close(c3); set(3, 'WindowStyle', 'normal')
92  end
93
94  % Drawing lines of left ventricle long axis
95  for i = 1:3
96      disp(['Draw line in figure ',num2str(i)]);
97      figure(i); set(i, 'WindowStyle', 'docked')
98      h = imline(gca(i)); pos = wait(h);
99
100     % Computing angle
101     dist = abs(diff(pos,1,1));
102     ang(i) = atan(dist(1)/dist(2));
```

```
103 end
104
105 % Finding center of image
106 img_center = (size(img) + 1) / 2;
107
108 % Adjusting frame of reference, so rotation happens around center
109 A1 = [1 0 0 0
110     0 1 0 0
111     0 0 1 0
112     -img_center 1];
113
114 % Construct affine transformation matrix (rotation)
115 A2 =  makehgtform('xrotate',ang(1),'yrotate',ang(2),'zrotate',ang(3))';
116
117 % Adjusting frame back to original
118 A3 = [1 0 0 0
119     0 1 0 0
120     0 0 1 0
121     img_center 1];
122
123 % Create MATLAB transformation structure
124 T = maketform('affine',A1*A2*A3);
```

A.4 Script for performing rotation - rot2sa

```
1  function rot_img = rot2sa(img,T,varargin)
2  % ROT_IMG = ROT2SA(IMG,T,varargin) Rotate image into short-axis view.
3  % Rotates an image or set of frames as defined by the com_rot ...
       function. The
4  % general MATLAB implementation is used, which requires several unused
5  % parameters to be defined.
6  % Last argument is an optional list of slices to be displayed.
7
8  % Copyright Andreas Clemmensen, 2012
9
10 % Pre-allocate
11 imgsize = size(img); %slices = [0, 0 , 0];
12 rot_img = zeros(size(img));
13
14 % Defining parameters for array transformation
15 R = makeresampler('cubic','bound');
16 TDIMS_A = [1 2 3]; TDIMS_B = [1 2 3];
17 TSIZE_B = imgsize(1:3);
18
19 disp('Rotating images... ');
20 % For multiple frames
21 if ndims(img) == 4
22     % Performing rotation on each bins
23     parfor i = 1:imgsize(4)
24         rot_img(:,:,:,i) = tformarray(img(:,:,:,i), T, R, TDIMS_A, ...
               TDIMS_B,...
25             TSIZE_B, [], 0);
```

```
    end
% For single (3D) frames
elseif ndims(img) == 3
    rot_img = tformarray(img, T, R, TDIMS_A, TDIMS_B,TSIZE_B, [], 0);
else
    error('FIPATO:rot2sa:InvalidParam','Input image must have 3 or ...
        4 dimensions');
end
disp(' done');

% Optional display of images with correct axis
if size(varargin,2) > 0
    slices = varargin{1};
    img_max = varargin{2};
    l_111 = linspace(-111*2.0364/2,111*2.0364/2,111);
    l_128 = linspace(-128*2.0364/2,128*2.0364/2,128);
    while any(slices)
        while any(slices(1))
            figure(4)
            imagesc(l_111,l_128,squeeze(rot_img(slices(1),:,:)));
            xlabel('[mm]'); ylabel('[mm]'); caxis([0 img_max]);
            title(['Coronal plane, slice no. ',num2str(slices(1))]);
            slices(1) = input('Coronal slice OK? ');
        end
        while any(slices(2))
            figure(5)
            imagesc(l_111,l_128,squeeze(rot_img(:,slices(2),:)));
            xlabel('[mm]'); ylabel('[mm]'); caxis([0 img_max]);
            title(['Sagittal plane, slice no. ',num2str(slices(2))]);
            slices(2) = input('Sigittal slice OK? ');
        end
        while any(slices(3))
            figure(6)
            imagesc(l_128,l_128,squeeze(rot_img(:,:,slices(3))));
            xlabel('[mm]'); ylabel('[mm]'); caxis([0 img_max]);
            title(['Transversal plane, slice no. ...
                ',num2str(slices(3))]);
            slices(3) = input('Transaxial slice OK? ');
        end
    end
end
```

A.5 Script for creating ROI - `draw_mask`

```
function voi = draw_mask(img)
% VOI = DRAW_MASK(IMG,L_SLICE,U_SLICE) Construct ROI for right ...
    ventricle.
% This function draws an region of interest (ROI) on the image ...
    (IMG), using
% the lower and upper slice limits defined as inputs.
%
% The function uses MATLAB enclosed tools for constructing the ...
```

```
    polygon. The
% output is a logical matrix

% Copyright Andreas Clemmensen, 2012

% Pre-allocate
close all;
voi = false(size(img)); % Logical matrix of zeros

% Create axis
l_111 = linspace(-111*2.0364/2,111*2.0364/2,111);
l_128 = linspace(-128*2.0364/2,128*2.0364/2,128);

% Defining initial range of shown values
base_CLim = [0 max(img(:))/10];
adj_CLim = base_CLim;

% Initial slice
slice = 50;

while any(slice)
    for i = 1:size(img,4)
        figure(i); set(i, 'WindowStyle', 'docked')
        imagesc(l_128,l_111,squeeze(img(:,slice,:,i)));
        xlabel('[mm]'); ylabel('[mm]'); colorbar;
        title(['Slice ',num2str(slice),', Gate ',num2str(i)]);
        % Setting range of values to pre-defined values
        set(gca,'CLim',adj_CLim);
    end
    c1 = imcontrast(1);
    slice = input('Slice OK? ');
    adj_CLim = get(get(1,'CurrentAxes'),'CLim');
end
close(c1);

% Draw intial ROI
disp('Draw ROI');
figure(1)



    % Creates ones inside polygon
    voi(i,:,:) = createMask(h);

    % Saves polygon for next slice
    pos = getPosition(h);

    % Close current slice
    close(k);
end
```

A.6 Script for constructing time-activity curve - `create_tac`

```
function tac = create_tac(img,voi)
%TAC = CREATE_TAC(IMG,VOI) creates a time-activity curve, showing the
% contrast bolus passing through the heart. A gamma-variate is ... fitted to the
% obtained data.

% Copyright Andreas Clemmensen, 2012

% Defining numbers and pre-allocate
bins = size(img,4); % Number of bins (frames)
tac = zeros(bins,1);
t = [1:bins]'; % Time axis

% Processing each frame
parfor i = 1:bins
    tempimg = squeeze(img(:,:,:,i)); % Isolate current frame
    tac(i) = mean(tempimg(voi)); % Compute activity in ROI
end

% Plotting datapoints
figure; plot(t,tac,'o'); grid on; hold on
xlabel('Time [s]'); ylabel('Mean activity [Bq/cc]');

% Defining gamma-variate function and starting values
modelFun =  @(p,t) p(3) .* (t - p(4)).^(p(1)) .* exp(-(t - p(4)) ./ ... p(2));
startingVals = [2 3 1.3e4 4];

% Performing non-linear fit
coefEsts = nlinfit(t, tac, modelFun, startingVals);

% Plotting fitted curve
xgrid = linspace(1,20,100);
line(xgrid, modelFun(coefEsts, xgrid), 'Color','r'); axis tight
```

A.7 Script for calculating RVEF - `calc_act`

```
function [act,EF] = calc_act(img,voi)
% [ACT,EF] = CALC_ACT(IMG,VOI) Calculate RVEF
% This function calculates the actual RVEF, using the reconstructed ... frames
% (IMG) and the ROI (VOI). The output is an vector of activity during
% cardiac cycle (ACT), and the calculated EF.

% Copyright Andreas Clemmensen, 2012

```

```
% Pre-allocate
bins = size(img,4);
act = zeros(bins,1);

% Looping over each bins (frame)
for i = 1:bins
    % Pulling out frame
    temp_frame = squeeze(img(:,:,:,i));
    % Finding activity inside ROI
    act(i) = sum(temp_frame(voi));
end

% EF = (EDV - ESV) / EDV
EF = (max(act)-min(act))/max(act);
disp(['RVEF = ' num2str(EF)]);
```